Bending-torsional coupled vibration of a rotor-bearing-system due to blade-casing rub in presence of non-uniform initial gap

Yang Yang[1*], Huajiang Ouyang[2], Xiaoli Wu[1], Yulin Jin[3], Yiren Yang[1], Dengqing Cao[4]

1. School of Mechanics and Engineering, Southwest Jiaotong University, Chengdu 610031, China
2. Centre for Engineering Dynamics, School Engineering, University of Liverpool, Liverpool L69 3GH, UK
3. School of Aeronautics and Astronautics, Sichuan University, Chengdu 610065, China
4. School of Astronautics, Harbin Institute of Technology, PO Box 137, Harbin 150001, China

Abstract: In most of investigations on rub, the initial gap between blades and casing is considered to be in uniform distribution around the circumstance. Actually, due to several factors, such as flight loads, thermal loads and coating inhomogeneity, the initial gap may be non-uniform. The aim of this paper is to gain insight into bending-torsional coupled vibration of a dynamic model of an aero engine subjected to blade-casing rub in presence of non-uniform initial gap. At first, a rotor-bearing-system is modelled, in which a non-uniform gap exists in on location or multiple locations. Utilizing the impact experiment performed at a rotor test rig, the Lankarani-Nikravesh model is proved to be able to reveal the impact mechanism between blades and casing under a non-uniform initial gap. In the tangential direction, the Coulomb model is applied to describe the friction characteristics at the contact points. After that the bending-torsional coupled vibration of the system is solved numerically and the response in the presence of a non-uniform gap is determined. Additionally, the effects of the features of the non-uniform initial gap are examined.

Keywords: Rotor-bearing system, bending-torsional coupled vibration, blade-casing rub, non-uniform initial gap.

1. Introduction

Performance and efficiency of rotating machines can be enhanced by reducing the clearance between components in relative motion, for example, reducing a rotor-stator gap is a current trend in industry [1-4]. However, this trend is likely to result in secondary issues such as rotor-stator contact interaction. Rub-impact fault could accelerate erosion and thermal fatigue. Furthermore, it may even cause the blades to break, the casing to fracture and other catastrophic failures in the worst cases [5, 6]. Thus, it is essential for engineers to determine dynamic characteristics of rotating machines with rub-impact in advance.

Rub-impact phenomenon is mainly caused by the rotor imbalance, misalignment, pedestal looseness, oil whip, thermal deformation and so on [7-10]. As for rotor-stator contact, there are three states of operating conditions: no rub, partial rub and full annular rub [11]. The so-called full annular rub refers to continuous contact between the rotor and the stator during the entire motion. While a partial rub refers to intermittent contact between the rotor and the stator, which may lead to speed fluctuation, severe wear and abnormal vibration to a great extent.

In the past years, two types of rub-impact fault (full annular rub and partial rub) have attracted a huge amount of interest already. Muszynska [12] gave a comprehensive literature survey on rotor-stator rub and reviewed various models. Jiang [13] analytically studied the global response characteristics of a piecewise smooth dynamical system with contact and gained deep insights into the interrelationships among parameters, such as coefficient of friction and stiffness ratio of rotor-to-stator stiffness. Chu et al. [14] observed that rich nonlinear phenomena, namely grazing bifurcation, quasi-periodic motion and chaotic motion, appeared in the vibration responses of a Jeffcott rotor system with partial rub. Cao et al. [15] proposed a fractional-order damped rotor system with partial

rub malfunction and then analysed various types of routes to chaos. Hong et al. [16] obtained a qualitative description of a non-smooth constraint due to the intermittent rub-impact process. On this basis, they discovered the potential effects of the non-smooth constraint on the modal features of the rotor system by theoretical and experimental methods. Zilli et al. [17] examined the forced responses of a two-degrees-of-freedom model of an unbalanced overhung rotor, in which the contact between rotor and stator was characterized by an intermittent type of behaviour. Zhang et al. [18] analysed the full annular rub motions of a nonlinear Jeffcott rotor. In reference [19], the forward and the backward full annular rub of a coupled rotor-stator system was studied analytically and the parameter ranges where the full annular rub occurred where determined as well. Fan et al. [20] presented a method for predicting a full annular rub, which might be hidden in start-up vibration of rotating machines. Besides, a number of important investigations [21-25] addressed rub-impact fault of a dual-rotor system and useful results revealing rub characteristics were obtained. In the above studies, it was generally assumed that the rub-impact fault happened between the rotor disc and the stator casing, where the rotor disc was regarded as a rigid one with mass imbalance.

As rub-impact fault often occurs, how to characterize the rubbing components more precisely is one of the key problems that need to be solved. Therefore, a more realistic form, i.e., blade-casing rub, is gradually recognized by more researchers [26]. Ma et al. [27] simplified the casing as a two-degrees-of-freedom model and studied single- and four-blade rubbings through numerical simulation and experiment. Aiming at the blade-casing rub, Padova et al. [28] studied the metal-to-metal contact due to sudden penetrations based on an in-ground spin-pit facility and considered the influences of different penetration depths. Sinha [29] proposed a flexible bladed rotor supported by a set of bearings at multiple locations and introduced Coulomb damping to describe the rubbing between the blade tips and the outer casing. Under the influence of blade-casing rub, Wang et al. [30] simulated the dynamic responses of a whole aero-engine for realizing fault diagnosis. Li et al. [31] derived an improved rotor dynamic model with blade-casing rub, in which the elastic deformations of both a single blade and casing were considered. A model of fully flexible bladed rotor was developed by Lesaffre et al. [32] and they studied the complete problem of contact between the flexible blades of the rotor and the flexible casing.

Up to now, the effects of non-uniform initial gap on the rub response of a rotor system have been rarely studied, even though the gap between blade tips and casing of a real aero engine is not uniform. Therefore, it is very important to include this feature in a proper rotor model if more realistic and useful results are required. This is the main contribution of this paper.

In rotor dynamics, there are two common modelling methods: continuous models and discrete models. In the former model, the components of rotating machines, such as discs, blades, shafts and drums, are seen as the classic beams, plates and shells [33-37]. The derived dynamic equations are usually expressed in partial differential forms. The latter discretize a rotor system into a number of simple parts, and the corresponding dynamic equations are ordinary differential ones. According to the discretization methods used, the latter can be further divided into three categories: the transfer matrix model [38], the finite element model [39] and the lumped mass model [40]. Compared with the other two, the lumped mass model could characterize the main features of complex rotating machines to a certain extent. And more importantly, there are generally not too many degrees of freedom in this kind of model, which is convenient for numerical calculation and theoretical analysis. All three main modes of rotor vibration – lateral, torsional and axial modes – may be present during rotor operation. Among these modes, the lateral modes of the rotor are of the greatest concern. However, torsional vibration is also important in practical rotors where unnoticed large torsional vibration can lead to serious failure. Thus, it is necessary to perform further investigations of lateral-torsional coupled motion of a rotor system in detail.

This paper aims at revealing the bending-torsional coupled vibration characteristics of a rotor system with blade-casing rub under a non-uniform initial gap. The structure of the paper is organized as follows: Firstly, the governing equation of motion of the rolling bearings-rotor system with blades

is established in Section 2. The rotor model, rolling bearing model, and non-uniform initial gap model are established; blade-casing rub experiment is reported and rub mechanism analysis is made in section. Next, the bending-torsional coupled vibration of the rotor system is analysed and the dynamic responses obtained under a uniform initial gap are compared with those under a non-uniform gap in Section 3. Moreover, a parametric analysis in terms of the non-uniform gap range, gap location and distribution is performed in Section 4. Finally, some conclusions are summarized in Section 5.

2. Dynamics modelling

To conduct a dynamic investigation of a rotating machine with rub malfunction, a comprehensive dynamic model is established in this paper. As shown in Fig. 1, this model is composed of a disc, eight straight blades, a flexible shaft, two rolling bearings and a casing. Due to the inherent nonlinearity introduced by the blade-casing contact, the model size has to be moderate to keep computational time reasonable. Therefore, during the dynamics modelling process, the following assumptions are made:

(1) The disc is treated as a rigid one and its deformation is ignored.

(2) Since the mass of the shaft is much smaller than that the disc, it is considered as a massless flexible body and its cross section is circular.

(3) Based on the structural design of the rotor test rig set up in the Aircraft Dynamics and Vibration Control Lab, Harbin Institute of Technology, the stiffness of the blades is much larger than that of the flexible shaft. Therefore, the elastic deformation of the blades is ignored.

(4) The lengths of all the blades are identical and the angle between any two adjacent blades is also identical. Meanwhile, the blades are rigidly mounted on the disc and the blade-loss event never happens.

(5) The casing support is seen as an ideal fixed support and the casing vibration is not taken into consideration.

(6) The thermal deformation of blades an casing is ignored.
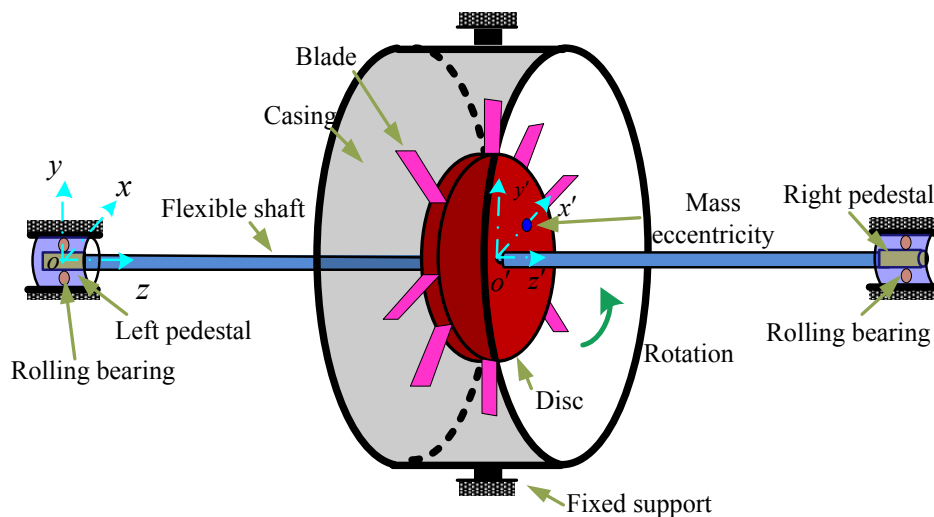
Fig. 1. Schematic diagram of rolling bearings-rotor system with straight blades.

2.1 Rotor model

There are three main parts in the rotor model: a left supporting pedestal, a rigid disc and a right supporting pedestal. The operating speeds of a large number of fan rotors are higher than their first critical speeds, but much lower than their second critical speeds. This means that only the first shaft mode is involved and the second mode will not be excited. Under this circumstance, when a disc is installed in the middle of a shaft [41], the gyroscopic effect of disc does not exist or is very weak.

With this in mind, two lateral degrees of freedom and one torsional degree of freedom are adopted here for the disc. In addition, two lateral degrees of freedom are used to describe the pedestal motion. Then, the dynamic equation of the rotor model containing a disc and two pedestals is derived in the following.

The global coordinate system is $o-xyz$, which is fixed to the Earth. And the local coordinate system is $o'-x'y'z'$, which rotates with the flexible shaft. Due to the existence of the eccentric disc mass, the rotor system is subjected to a centrifugal force, which leads to whirling motion. During this process, the kinetic energy of the system includes that of disc T_d, that of eccentric mass T_e, and those of two pedestals T_{ls} and T_{rs}.
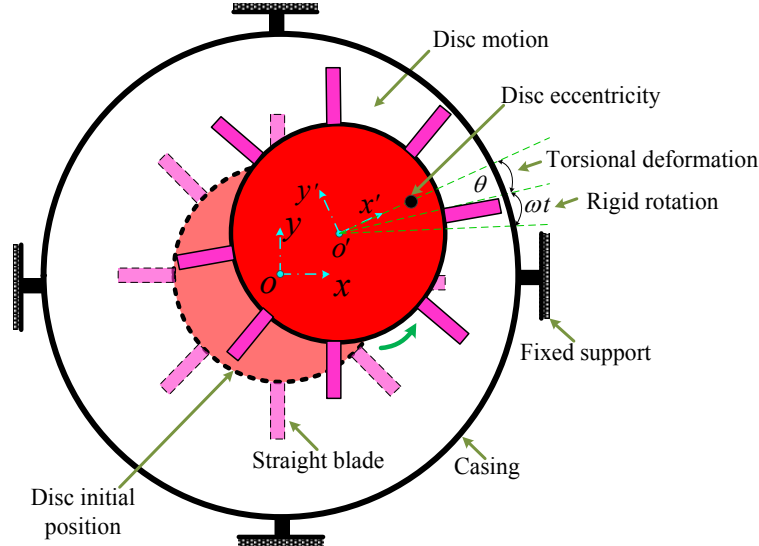
Fig. 2. Whirling motion and torsional motion of the rotor system with blades.

The equivalent mass and the equivalent rotational inertia of the disc with blades are defined as m_d and J_0. Thus, the kinetic energy of the disc with blades can be expressed as

$$T_d = \frac{1}{2}m_d\left(\dot{x}_d^2 + \dot{y}_d^2\right) + \frac{1}{2}J_0\dot{\varphi}_d^2, \tag{1}$$

where $\dot{x}_d$ and $\dot{y}_d$ denote the disc's lateral velocity and vertical velocity, respectively.

It is obvious from Fig. 2 that the disc rotation φ_d consists of the rigid body rotation ωt and the angle of twist θ. Therefore

$$\begin{cases} \varphi_d = \theta + \omega t, \\ \dot{\varphi}_d = \dot{\theta} + \omega, \end{cases} \tag{2}$$

where $\dot{\theta}$ denotes the torsional velocity of the disc and ω denotes the shaft speed.

Since an imbalance mass exists in the rigid disc, the displacement and the velocity of this imbalance mass can be expressed as

$$\begin{cases} x_e = x_d + e\cos\varphi_d, \\ y_e = y_d + e\sin\varphi_d, \\ \dot{x}_e = \dot{x}_d - e\dot{\varphi}_d\sin\varphi_d, \\ \dot{y}_e = \dot{y}_d + e\dot{\varphi}_d\cos\varphi_d, \end{cases} \tag{3}$$

where e denotes the disc eccentricity. Similarly, the kinetic energy of the imbalance mass can also be expressed as

$$T_e = \frac{1}{2}m_e\left(\dot{x}_e^2 + \dot{y}_e^2\right). \tag{4}$$

In addition, the kinetic energy expressions of the left supporting pedestal and the right supporting pedestal are further given as

$$\begin{cases} T_{ls} = \dfrac{1}{2}m_{ls}\dot{x}_{ls}^2 + \dfrac{1}{2}m_{ls}\dot{y}_{ls}^2, \\[3mm] T_{rs} = \dfrac{1}{2}m_{rs}\dot{x}_{rs}^2 + \dfrac{1}{2}m_{rs}\dot{y}_{rs}^2, \end{cases} \tag{5}$$

where m_{ls} and m_{rs} denote the left pedestal mass and the right pedestal mass, $\dot{x}_{ls}$ and $\dot{x}_{rs}$ denote the velocities of the two pedestals in the lateral direction, $\dot{y}_{ls}$ and $\dot{y}_{rs}$ denote the velocities of the two pedestals in the vertical direction, respectively.

After obtaining Eqs. (1), (4) and (5), the kinetic energy of the rotor system is written in the following form.

$$T = \frac{1}{2}m_d\left(\dot{x}_d^2 + \dot{y}_d^2\right) + \frac{1}{2}J_0\dot{\varphi}_d^2 + \frac{1}{2}m_e\left(\dot{x}_e^2 + \dot{y}_e^2\right) + \frac{1}{2}m_{ls}\dot{x}_{ls}^2 + \frac{1}{2}m_{ls}\dot{y}_{ls}^2 + \frac{1}{2}m_{rs}\dot{x}_{rs}^2 + \frac{1}{2}m_{rs}\dot{y}_{rs}^2. \tag{6}$$

Based on the assumptions (1) and (3), the elastic deformations of the blades and the disc are ignored, that is to say, all the elastic deformations of the rotor system mainly concentrate on the lateral and torsional deformation of the flexible shaft. Therefore, the potential energy expression of the rotor system obeys

$$V = \frac{1}{2}k_b\left(x_d - x_{ls}\right)^2 + \frac{1}{2}k_b\left(x_{rs} - x_d\right)^2 + \frac{1}{2}k_b\left(y_d - y_{ls}\right)^2 + \frac{1}{2}k_b\left(y_{rs} - y_d\right)^2 + \frac{1}{2}k_t\left(\varphi_d - \omega t\right)^2, \tag{7}$$

where k_b denotes the shaft's lateral stiffness due to bending, k_t denotes the shaft's torsional stiffness, x_{ls} and x_{rs} denote the lateral displacements of the two pedestals, y_{ls} and y_{rs} denote the vertical displacements of the two pedestals, respectively.

The lateral and vertical damping, and the torsional damping are introduced to the rotor system. And then the dissipated energy during the whirling motion and the torsional motion can be expressed as

$$D = \frac{1}{2}c_b\left(\dot{x}_d - \dot{x}_{ls}\right)^2 + \frac{1}{2}c_b\left(\dot{x}_{rs} - \dot{x}_d\right)^2 + \frac{1}{2}c_b\left(\dot{y}_d - \dot{y}_{ls}\right)^2 + \frac{1}{2}c_b\left(\dot{y}_{rs} - \dot{y}_d\right)^2 + \frac{1}{2}c_t\left(\dot{\varphi}_d - \omega\right)^2, \tag{8}$$

in which, c_b denotes the shaft's lateral damping, c_t denotes the shaft's torsional damping.

By utilizing Eqs. (6-8), the dynamic equation of the rolling bearings-rotor system with blades is given in matrix form below. The detailed derivations of the terms used in the Lagrange's equation are provided in Appendix A.

$$\mathbf{M}\ddot{\mathbf{u}} + \mathbf{C}\dot{\mathbf{u}} + \mathbf{K}\mathbf{u} = \mathbf{F}_g, \tag{9}$$

where the generalized displacement vector is $\mathbf{u}^T = \left[x_d, y_d, \theta, x_{ls}, y_{ls}, x_{rs}, y_{rs}\right]^T$, which indicates that the dynamic model established in this paper has 7 degrees of freedom. The mass matrix $\mathbf{M}$, damping matrix $\mathbf{C}$ and stiffness matrix $\mathbf{K}$ are respectively derived as

$$\mathbf{M} = \begin{bmatrix} m_d + m_e & 0 & -m_e e\sin\left(\omega t + \theta\right) & 0 & 0 & 0 & 0 \\ 0 & m_d + m_e & m_e e\cos\left(\omega t + \theta\right) & 0 & 0 & 0 & 0 \\ -m_e e\sin\left(\omega t + \theta\right) & m_e e\cos\left(\omega t + \theta\right) & J_0 + m_e e^2 & 0 & 0 & 0 & 0 \\ 0 & 0 & 0 & m_{ls} & 0 & 0 & 0 \\ 0 & 0 & 0 & 0 & m_{ls} & 0 & 0 \\ 0 & 0 & 0 & 0 & 0 & m_{rs} & 0 \\ 0 & 0 & 0 & 0 & 0 & 0 & m_{rs} \end{bmatrix}, \tag{10}$$

$$
\mathbf{C}=
\begin{bmatrix}
2c_b & 0 & 0 & -c_b & 0 & -c_b & 0 \\
0 & 2c_b & 0 & 0 & -c_b & 0 & -c_b \\
-m_e e\left(\omega+\dot\theta\right)\cos\left(\omega t+\theta\right) & -m_e e\left(\omega+\dot\theta\right)\sin\left(\omega t+\theta\right) & c_t & 0 & 0 & 0 & 0 \\
-c_b & 0 & 0 & c_b & 0 & 0 & 0 \\
0 & -c_b & 0 & 0 & c_b & 0 & 0 \\
-c_b & 0 & 0 & 0 & 0 & c_b & 0 \\
0 & -c_b & 0 & 0 & 0 & 0 & c_b
\end{bmatrix},
\tag{11}
$$

$$
\mathbf{K}=
\begin{bmatrix}
2k_b & 0 & 0 & -k_b & 0 & -k_b & 0 \\
0 & 2k_b & 0 & 0 & -k_b & 0 & -k_b \\
0 & 0 & k_t & 0 & 0 & 0 & 0 \\
-k_b & 0 & 0 & k_b & 0 & 0 & 0 \\
0 & -k_b & 0 & 0 & k_b & 0 & 0 \\
-k_b & 0 & 0 & 0 & 0 & k_b & 0 \\
0 & -k_b & 0 & 0 & 0 & 0 & k_b
\end{bmatrix}.
\tag{12}
$$

For the rotor system shown in Fig. 1, it is subjected to the centrifugal force caused by the disc imbalance and the constraint force provided by the rolling bearings. If blade-casing rub happens, a rub-impact force and a friction torque act on the rotor system. Therefore, the generalized force matrix $\mathbf{F_g}$ in Eq. (9) can be expressed as

$$
\mathbf{F_g}=
\begin{bmatrix}
F_x+F_{ex} \\
F_y+F_{ey} \\
M \\
F_{blx} \\
F_{bly} \\
F_{brx} \\
F_{bry}
\end{bmatrix},
\tag{13}
$$

where F_x and F_y denote the two components of rub-impact force in the directions of $o-x$ and $o-y$. Meanwhile, M denotes the friction torque, F_{blx} and F_{bly} denote the two supporting forces of the left pedestal, and F_{brx} and F_{bry} denote the two supporting forces of the right pedestal. Their mathematical expressions will be given later.

In Eq. (13), variables F_{ex} and F_{ey} can be seen as two components of imbalance force acting on the rotor system and they are

$$
\begin{cases}
F_{ex}=m_e e\left(\omega+\dot\theta\right)^2\cos\left(\omega t+\theta\right), \\
F_{ey}=m_e e\left(\omega+\dot\theta\right)^2\sin\left(\omega t+\theta\right),
\end{cases}
\tag{14}
$$

Obviously, these two components are closely related to the rotor speed, torsional velocity and disc eccentricity. In the following sections, the rolling bearing model and the rub-impact force model are introduced.

2.2 Rolling bearing model

As shown in Fig. 3, the rolling bearing model consists of bearing inner ring, bearing outer ring,

rolling balls. The bearing outer ring is fixed in the bearing chock and the bearing inner ring is mounted on the shaft. The cage in this model has no mass but could be considered as a geometric constraint that keeps the rolling balls evenly arranged on the circumference

According to references [42], another assumption is made that the balls are only rolling and no sliding occurs, where the deformation of the bearing is mainly contact deformation between the rolling balls and the raceway. In Fig. 3, R_b and r_b represent the radii of the bearing inner and outer orbits, respectively. Therefore, the rotational speed of the cage can be expressed as

$$\omega_{cage} = \frac{2v_{cage}}{R_b + r_b} = \frac{v_{outer} + v_{inner}}{R_b + r_b} = \frac{\omega r_b}{R_b + r_b},$$ (15)

According to Eq. (15), the angle of the jth rolling ball at t moment is calculated as

$$\begin{cases} \phi_j = \omega_{cage} \times t + \frac{2\pi}{N_r}(j-1), \\ j = 1, 2, \ldots, N_r, \end{cases}$$ (16)

in which, N_r denotes the number of rolling balls.
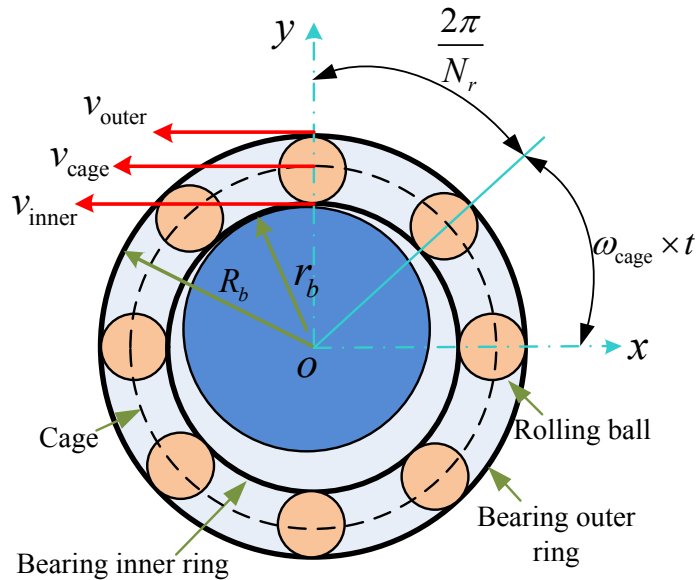
Fig. 3. Schematic diagram of a rolling bearing model.

According to Eq. (16), the contact deformation for the jth rolling ball is given by

$$u_j = x_r \cos\phi_j + y_r \sin\phi_j - r_0,$$ (17)

where x_r and x_r denotes the lateral and vertical displacements of the pedestal, r_0 denotes the initial clearance of the rolling bearing.

The elastic contact between rolling balls and raceway yields a nonlinear force-deformation relationship that can be described by the Hertz theory [43]. Therefore, the expression of the contact force between the jth rolling ball and the raceway is written as

$$F_{bj} = C_b H(u_j) u_j^{\frac{3}{2}},$$ (18)

where C_b is the contact stiffness coefficient, which depends on the contact geometry and the elastic materials in contact. The Heaviside function $H(u_j)$ obeys the following form

$$H(u_j) = \begin{cases} 1, & u_j > 0 \\ 0. & u_j \leq 0 \end{cases}$$ (19)

The total restoring force acting on the bearing is the sum of all forces from the individual rolling

balls. Here, the two components of the total restoring forces in the $o-x$ axis and the $o-y$ axis can be further obtained, namely

$$\begin{cases} F_{bx} = \sum_{j=1}^{N_r} F_{bj} \cos\phi_j, \\[2ex] F_{by} = \sum_{j=1}^{N_r} F_{bj} \sin\phi_j. \end{cases} \tag{20}$$

Substituting the displacements of the left and right pedestals into Eq. (20), the supporting forces of the two pedestals F_{blx}, F_{bly}, F_{brx}, and F_{bry} can be respectively obtained.

2.3 Mathematic function of non-uniform initial gap

As introduced in reference [44], improved sealing in high pressure turbines (HPT) can provide a dramatic reduction in fuel consumption, as well as increased payload and mission range capabilities. For the modern aviation industry, coatings have been widely applied to the component surfaces for gas path sealing, oxidation and corrosion control [45]. Initial gap control is achieved by coating the casing liner with an abrasive coating layer and the blade tip with an abrasive layer.

A cross section of the combustor and two-stage HPT of an engine is shown in Fig. 4, in which the turbine disc, straight blades and tip seal of the first-stage turbine are labelled [46]. According to the illustration given in [46], it is known that the initial gap between the blades and the casing may become non-uniform under the influences of flight load (i.e., inertial load and aerodynamic load), thermal load and coating inhomogeneity. These will inevitably affect the blade-casing rub and even interfere with the normal operation of these rotating machines.
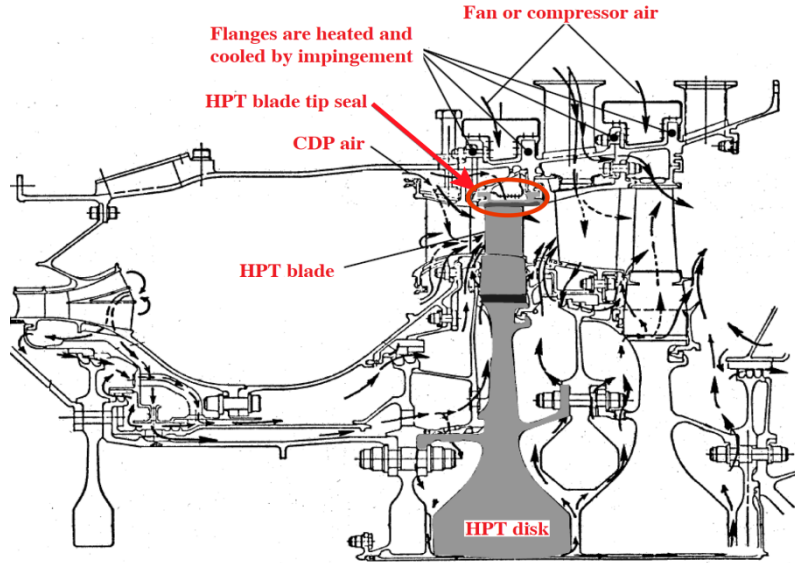

Fig. 4. HPT blade tip seal location in a modern gas turbine engine [46].

Two configurations of rotor-casing with sealing coating are depicted in Fig. 5, which contains a uniform initial gap and a non-uniform initial gap. In Fig. 5(a), the uniform initial gap is set to δ_0 and then the rub condition is exactly the same as described in some previous works [47-50]; that is to say, when the radial displacement of the rotor system is larger than the initial gap δ_0, rub-impact fault will happen.

Fig. 5(b) shows the case of a non-uniform initial gap, where the magnitude and the range of the gap at multiple locations may not be consistent. Therefore, rub condition corresponding to the non-uniform gap is more complicated than that corresponding to the uniform gap, and it is more likely to disturb the smooth operation of a rotating machine.

a) uniform initial gap   b) non-uniform initial gap
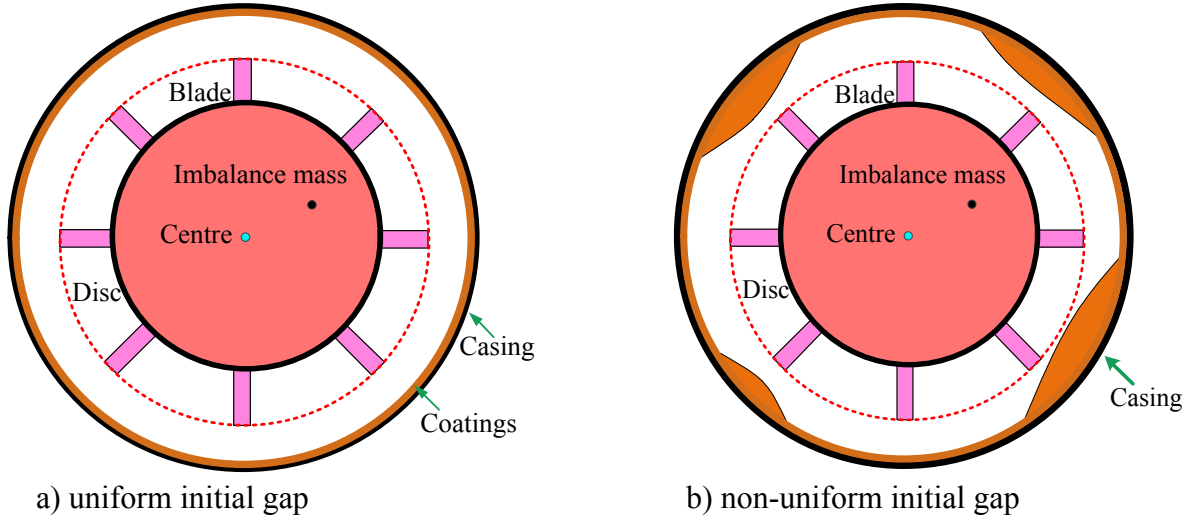
Fig. 5. Two configurations of rotor-casing with sealing coating: (a) uniform initial gap and (b) non-uniform initial gap.

If there are N uniformly distributed blades on the rigid disc, the angle between the ith blade and the $o-x$ axis at time t is given as

$$\theta_{bi} = \frac{2\pi}{N}(i-1) + \omega t + \theta. \tag{21}$$

Obviously, the angular position of the blade includes the torsional deformation of the disc. Therefore, the effect of torsional deformation on the rub-impact between blade and casing is considered in this paper. The inner relation between them is further given in subsection 2.4.

On this basis, a cosine function given in reference [51] is introduced to the rotor system for describing the non-uniform gap. As shown in Fig. 6(a), the location and range of the non-uniform gap are defined by α and β, respectively. δ_{max} is used to describe the maximum magnitude of the non-uniform gap. Meanwhile, the spatial variation of the initial gap is conceptually divided into three segments, as shown in Fig. 6(b).
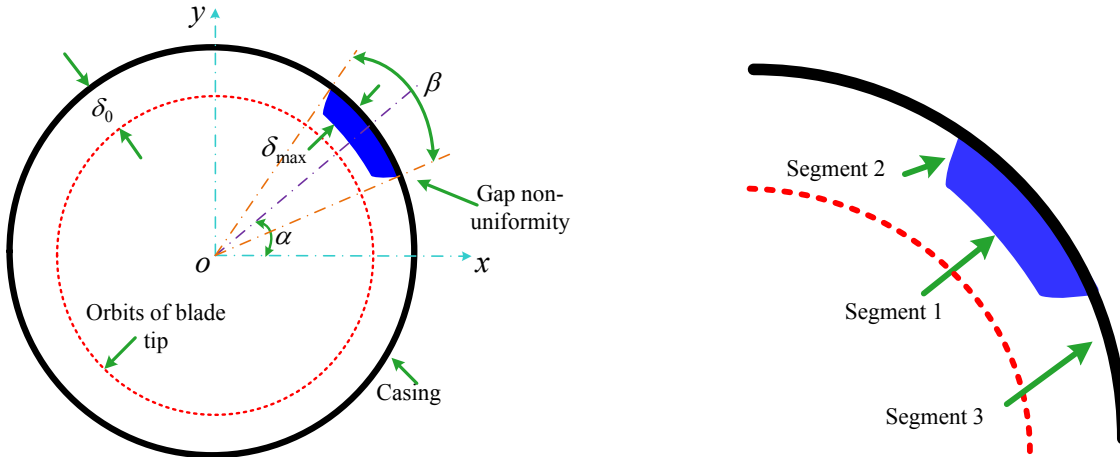
a) illustration of variables describing the non-uniform gap   b) three segments in the non-uniform gap

Fig. 6. Schematic diagram of the non-uniform gap: (a) illustration of variables describing the non-uniform gap and (b) three segments in the non-uniform gap.

Thus, the initial gap between the ith blade and the casing at time t can be expressed as

$$\delta(\theta_{bi}) = \begin{cases} \delta_0 - \delta_{max}, & |\theta_{bi} - \alpha| < \dfrac{\beta}{2} & \text{(Segment 1)} \\[2mm] \delta_0 - \delta_{max}\left[0.5 - 0.5\cos\dfrac{2\pi(\theta_{bi}-\alpha)}{\beta}\right], & \dfrac{\beta}{2} < |\theta_{bi}-\alpha| < \beta & \text{(Segment 2)} \\[2mm] \delta_0, & |\theta_{bi}-\alpha| > \beta & \text{(Segment 3)} \end{cases} \qquad (22)$$

In order to understand the mathematic function describing the non-uniform initial gap more comprehensively, a parametric analysis of two quantities δ_{max} and β is performed in the following part, where the structural parameters of the rotor system are taken from reference [52] and listed in Appendix B.
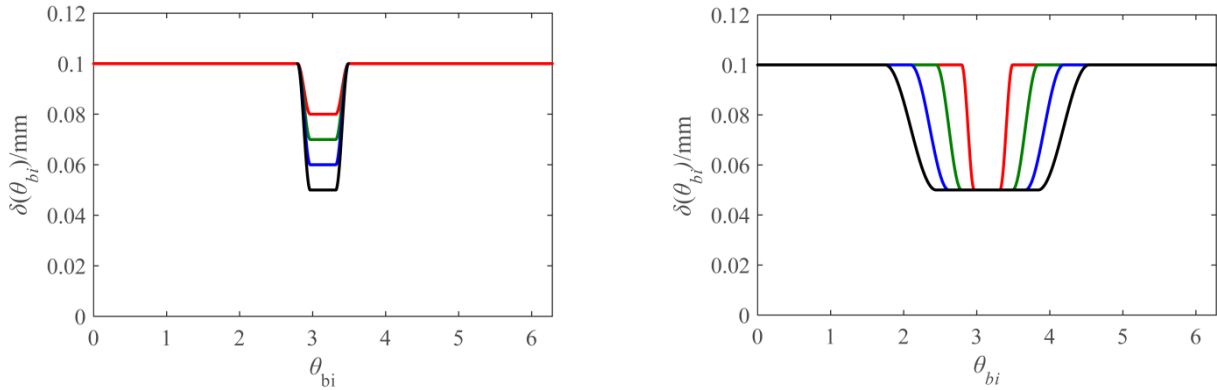
a) different maximum magnitudes of non-uniform gap

b) different ranges of non-uniform gap

Fig. 7. Variation of initial gap between blades and casing reflected by key variables: (a) different maximum magnitude of non-uniform gap δ_{max} and (b) different ranges of non-uniform gap β.

Assume that there is only one non-uniform gap at $\alpha = \pi$ rad/s and the other parameters remain constant. When the maximum magnitude of the non-uniform gap is set to $\delta_{max} = [0.02,\ 0.03,\ 0.04,\ 0.05]$ mm, the change of the initial gap $\delta(\theta_{bi})$ is shown in Fig. 7(a). Moreover, the variation in the ranges of the initial gap is also given in Fig. 7(b), which are $\beta = [\pi/9,\ 2\pi/9,\ 3\pi/9,\ 4\pi/9]$ rad. From these two figures, it can be seen that an increase of δ_{max} or β represents a more severe non-uniform gap.
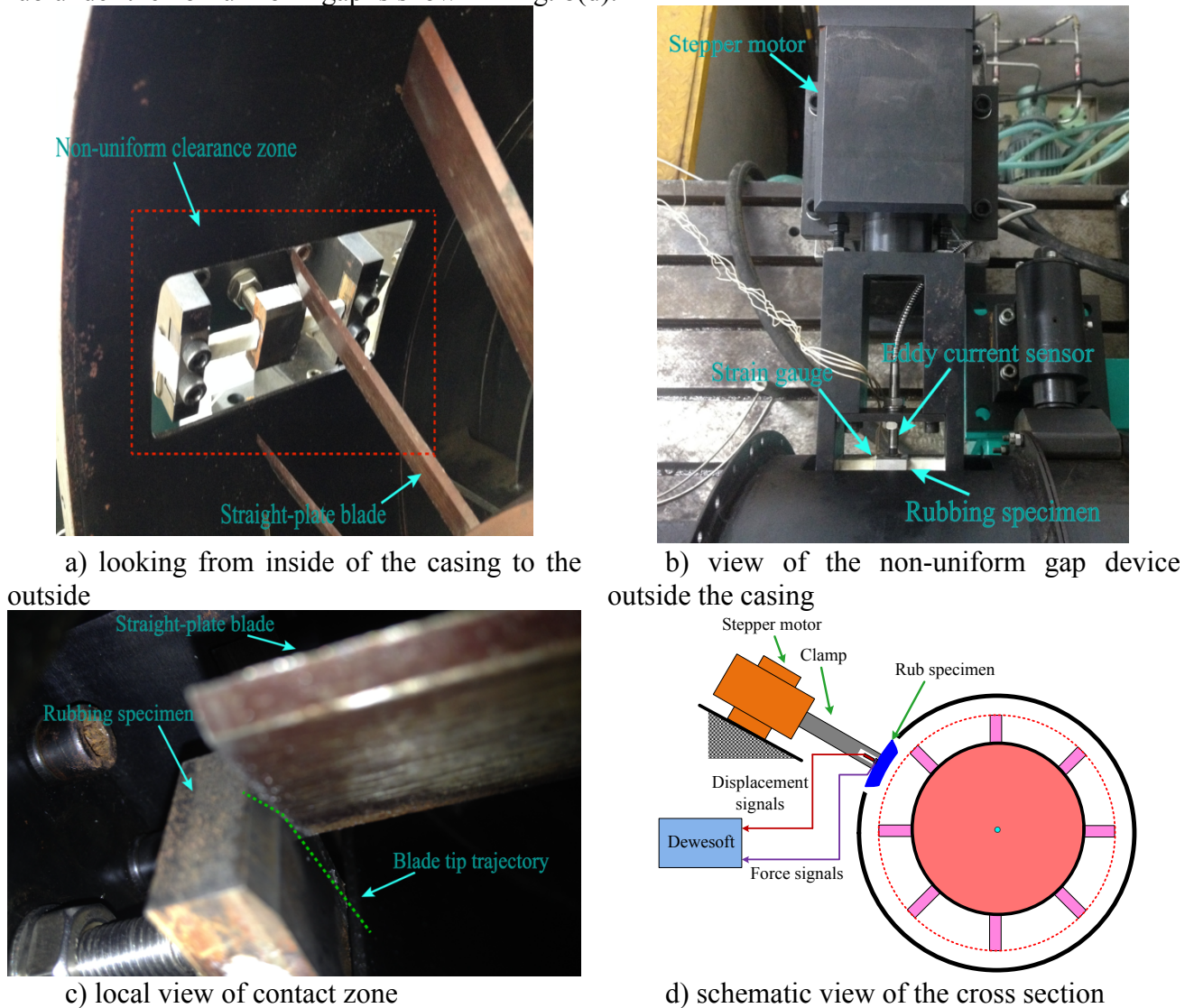
2.4 Mechanism of blade-casing rub

Considering the non-uniform initial gap, the mechanism of blade-casing rub is investigated in this section. By combining rub experiment with theoretical analysis, the expressions of rub-impact force and friction torque acting on the rotor system (see Eq. (13)) are established in detail.

To perform the investigation of blade-casing rub, an experimental rig is established in the Aircraft Dynamics and Vibration Control Lab. As shown in Fig. 8(a), an opening on the casing is made for installing a particular device for implementing the non-uniform gap. Similar to the theoretical model, the several straight blades are installed on the compressor disc and the lengths of all the blades are identical. Therefore, when the radial displacement of the rotor is larger than the initial gap, blade-casing rub occurs.

Fig. 8(b) is the view of the non-uniform gap device outside casing. From this figure, it can be seen that the rub specimen is mounted on a clamp. The bottom of the clamp is connected to the stepper motor, which can increase the initial gap when turning in its normal direction but decrease the initial gap when turning in its reverse direction. Therefore, the magnitude of the non-uniform gap

can be adjusted flexibly in the experiment. As for signal acquisition, the eddy current sensor and the strain gauges are used to measure the impact displacement and the impact force, respectively. When the blades rub against the specimen, the trajectory of blade tip is illustrated in Fig. 8(c). In order to achieve the consistency between the theoretical analysis and the experiment, the shape of the specimen is similar to that basin-like curve given in Fig. 7. The principal diagram of the blade-casing rub under the non-uniform gap is shown in Fig. 8(d).

a) looking from inside of the casing to the outside

b) view of the non-uniform gap device outside the casing

c) local view of contact zone

d) schematic view of the cross section

Fig. 8. Experimental rig of blade-casing rub under non-uniform gap: (a) looking from inside of the casing to the outside, (b) view of the non-uniform gap device outside the casing, (c) local view of contact zone, and (d) schematic view of the cross section.

At rotor speeds of $600\,\mathrm{rpm}$ and $900\,\mathrm{rpm}$, the relations between impact displacement and impact force are respectively shown in Fig. 9(a) and Fig. 9(c). Due to the loss of the mechanical energy caused by impact damping, hysteretic loops are formed. By comparing these two figures, it can also be observed that both the maximum impact force and the maximum impact displacement rise with the increase of rotor speed.

To describe the blade-casing impact mechanism under the non-uniform gap, the Lankarani-Nikravesh model [53, 54] is introduced which was developed based on the Hertz contact theory and accounts for a number of features, such as local contact area, material characteristics, energy loss and so on. The expression of the Lankarani-Nikravesh model is

$$F=\begin{cases}k_p\delta^{\frac{3}{2}}\left(1+\dfrac{3\left(1-c_e^2\right)\dot{\delta}}{4\dot{\delta}_p^-}\right), & \delta\geq0\\[3mm]0, & \delta<0\end{cases}\tag{23}$$

where k_p denotes the impact stiffness, c_e denotes the coefficient of restitution, $\dot{\delta}_p^-$ represents the initial impact velocity.

a) experimental data b) theoretical data

c) experimental data d) theoretical data
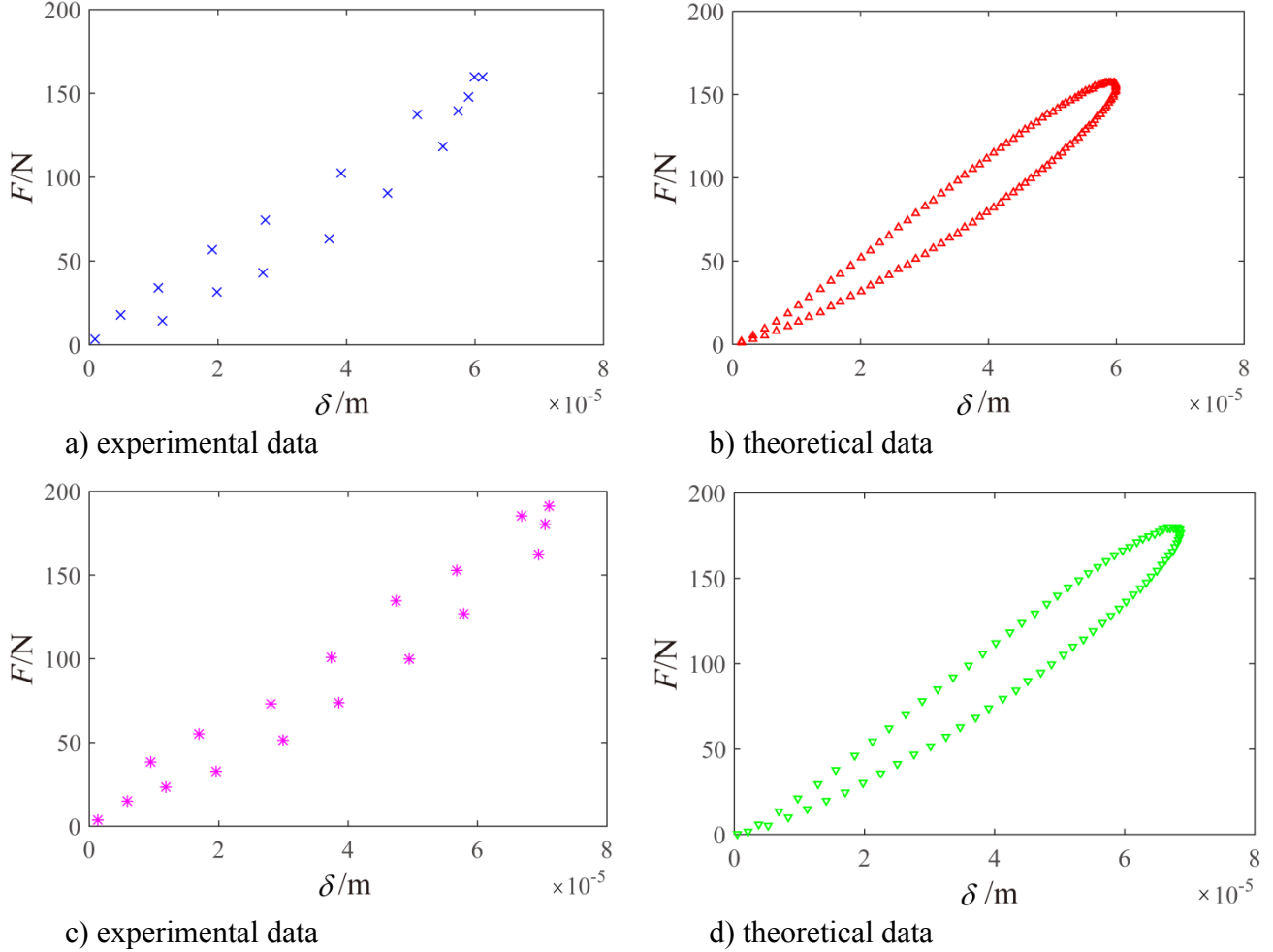
Fig. 9. Relation between impact force and impact displacement: (a) experimental data at $\omega=600$ rpm, (b) theoretical data at $\omega=600$ rpm, (c) experimental data at $\omega=900$ rpm, and (d) theoretical data at $\omega=900$ rpm.

As a consequence, the theoretical results for describing the relationship of impact force-impact displacement are shown in Fig. 9(b) and Fig. 9(d), where the coefficient of restitution is $c_e=0.9$. Overall, the theoretical results and experimental results are well matched at the two rotor speeds. This illustrates that the Lankarani-Nikravesh model could capture the impact mechanism under the non-uniform gap to some extent.

The tangential friction force is governed by both the normal impact force and the coefficient of friction, and it is given by

$$T=\begin{cases}\mu\,\mathrm{sgn}\left(v_{rel}\right)k_p\delta^{\frac{3}{2}}\left(1+\dfrac{3\left(1-c_e^2\right)\dot{\delta}}{4\dot{\delta}_p^-}\right), & \delta\geq0\\[3mm]0, & \delta<0\end{cases}\tag{24}$$

where the coefficient of friction μ is mainly determined by the surface condition of the sealing coating. Moreover, the sgn function depends on the tangential relative velocity between the two surfaces at the contact point of blade-casing.

For the ith blade and the casing shown in Fig. 10(a), the tangential relative velocity v_{rel} at the contact point can be expressed as

$$v_{rel} = \left(\omega + \dot{\theta}\right)\left(R_d + l_{bi}\right) + \dot{y}_d \cos\theta_{bi} - \dot{x}_d \sin\theta_{bi}, \tag{25}$$

in which R_d is the disc radius and l_{bi} is the length of the ith blade.

The above expression indicates that the tangential relative velocity depends on the shaft speed, whirling velocity and twist velocity. Moreover, the blade-casing rub and the rotor dynamic behaviour are closely coupled.
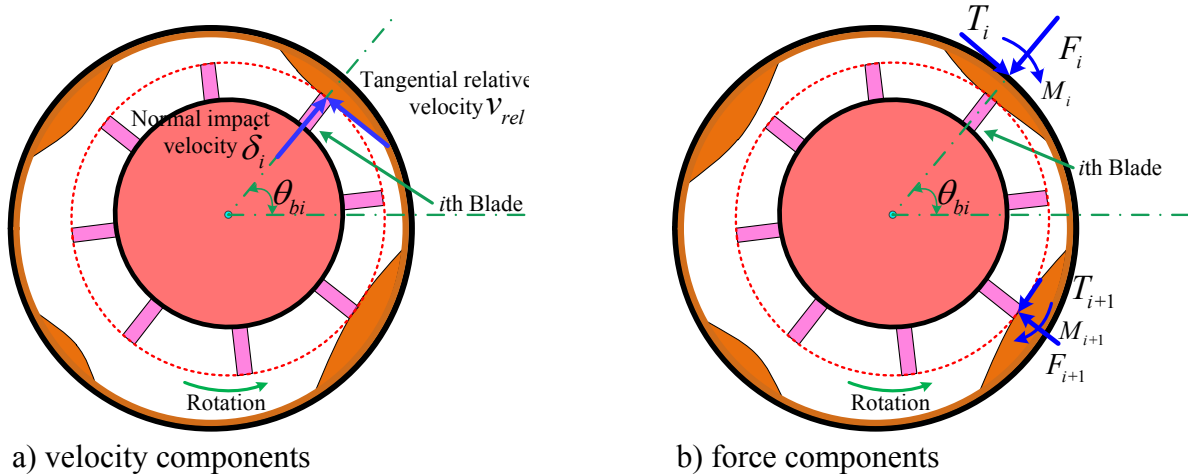
a) velocity components   b) force components

Fig. 10. Diagram of blade-casing rub under the non-uniform initial gap: (a) velocity components and (b) force components.

Meanwhile, the impact displacement δ_i and the impact velocity $\dot{\delta}_i$ of the ith blade in the normal direction are given by

$$\begin{cases} \delta_i = x_d \cos\theta_{bi} + y_d \sin\theta_{bi} - \delta\left(\theta_{bi}\right), \\ \dot{\delta}_i = \dot{x}_d \cos\theta_{bi} + \dot{y}_d \sin\theta_{bi}. \end{cases} \tag{26}$$

Substituting Eqs. (25) and (26) into Eqs. (23) and (24), the rub force components (i.e., impact force F_i, friction force T_i and friction torque M_i) between the ith blade and the casing can be expressed as

$$\begin{cases} F_i = k_p \delta_i^{\frac{3}{2}}\left(1 + \dfrac{3\left(1 - c_e^2\right)\dot{\delta}_i}{4\dot{\delta}_p^-}\right), \\ T_i = F_i \mu \, \text{sgn}\left(v_{rel}\right), \\ M_i = T_i\left(R_d + l_{bi}\right). \end{cases} \tag{27}$$

Consequently, for the rotor system established in this paper, the total rub force is the sum of the rub forces acting on the rotating blades, as shown in Fig. 10(b). On this basis, the normal forces, tangential forces and friction torques may be transformed as the external forces in Eq. (13) by using the following geometric relations:

$$\begin{cases} F_x = \sum_{i=1}^{N}\left(-F_i\cos\theta_{bi}+T_i\sin\theta_{bi}\right), \\[2mm] F_y = \sum_{i=1}^{N}\left(-F_i\sin\theta_{bi}-T_i\cos\theta_{bi}\right), \\[2mm] M = -\sum_{i=1}^{N}M_i. \end{cases} \tag{28}$$

2.5 Identification of maximum impact deformation

The rub experiment proves that although the phenomenon of energy loss exists in the rub process, it is much less than the mechanical energy of the rotor system. For studying the maximum impact deformation analytically, the energy loss is not considered in this section. And then the Lankarani-Nikravesh model can be reduced to the Hertz model.

According to the energy conservation principle, the total energy of the system before collision is equal to that after collision, namely

$$\frac{1}{2}k_b\left(\delta_0-\delta_{max}\right)^2+\frac{1}{2}\left(m_d+m_e\right)\left(\dot\delta_p^-\right)^2=\frac{1}{2}k_b\left(\delta_0-\delta_{max}+\delta_{p,m}\right)^2+\int_0^{\delta_{p,m}}k_p\delta^{\frac{3}{2}}d\delta, \tag{29}$$

where $\delta_0-\delta_{max}$ denotes the non-uniform initial gap, and $\delta_{p,m}$ denotes the maximum impact deformation between a single blade and casing.

Through a further analysis, the implicit expression between $\delta_{p,m}$ and $\dot\delta_p^-$ is satisfied when

$$\frac{4k_p}{5\left(m_d+m_e\right)}\delta_{p,m}^{\frac{5}{2}}+\frac{k_b}{m_d+m_e}\delta_{p,m}^2+\frac{2k_b\left(\delta_0-\delta_m\right)}{m_d+m_e}\delta_{p,m}-\left(\dot\delta_p^-\right)^2=0. \tag{30}$$

If the Hertz model is replaced by a piecewise linear stiffness model, the above implicit expression becomes

$$\frac{2k_b\left(\delta_0-\delta_{max}\right)}{m_d+m_e}\delta_{p,m}+\frac{k_b+k_p}{m_d+m_e}\delta_{p,m}^2-\left(\dot\delta_p^-\right)^2=0. \tag{31}$$

Note that the effect of the non-uniform initial gap has been considered in Eqs. (30) and (31). Assume that the initial gap between the blades and the casing is extremely small, and then Eq. (31) may be further reduced as

$$\frac{k_b+k_p}{m_d+m_e}\delta_{p,m}^2-\left(\dot\delta_p^-\right)^2=0. \tag{32}$$
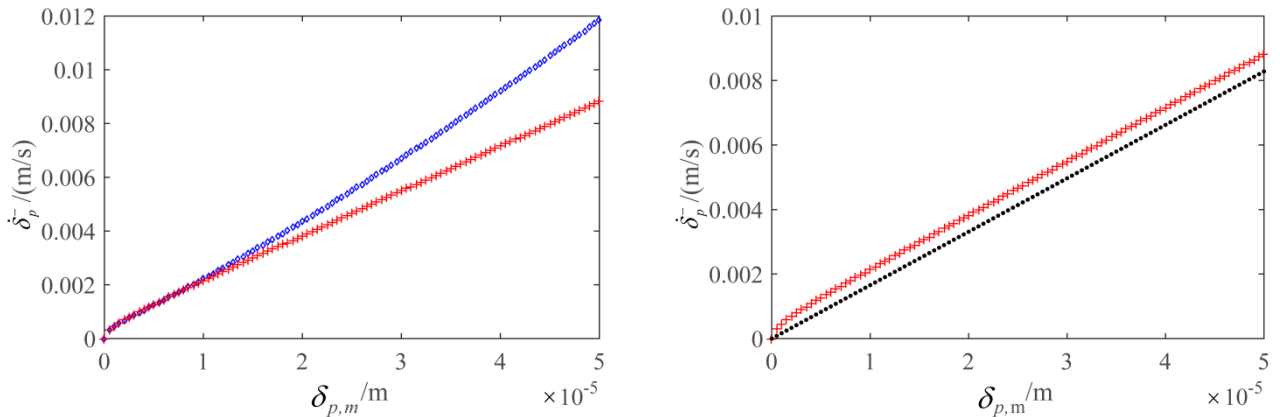
a) using the Hertz model and the piecewise linear model

b) with or without the initial gap

Fig. 11. Relation between $\delta_{p,m}$ and $\dot\delta_p^-$: (a) using the Hertz model and the piecewise linear model,

and (b) with or without the initial gap.

Let the maximum impact deformation between a single blade and the casing varies as $\delta_{p,m}=[0:0.05:5]\times10^{-5}$ m and the above three implicit equations are solved numerically. As shown in Fig. 11(a), with the increase of $\delta_{p,m}$, the difference between the Hertz model (blue line) and the piecewise linear stiffness model (red line) gradually becomes larger. For the cases with or without an initial gap, the difference of initial impact velocity between them remains unchanged, in which the red line represents the results considering the initial gap and the black line represents the results without an initial gap.

3. Simulation and discussion

The dynamical simulation of Eq. (9) is carried out by using the fourth-order Runge-Kutta method with the consideration of blade-casing rub fault under non-uniform gap. During the direct numerical integration, the time step is specified as $2\pi/(1000\omega)$. Fig. 12 shows the simulation flow chart, in which there are four parts, including a main procedure and three subroutines. The main procedure is used to implement the dynamic model and solve the vibration response at each time instant. Subroutine 1 is used to calculate the support forces of the two rolling bearings. Subroutine 2 is utilized to describe the non-uniform initial gap, including its range, the location and the magnitude. Subroutine 3 is utilized to simulate the impact force, friction force and friction torque between the rotating blades and the casing.
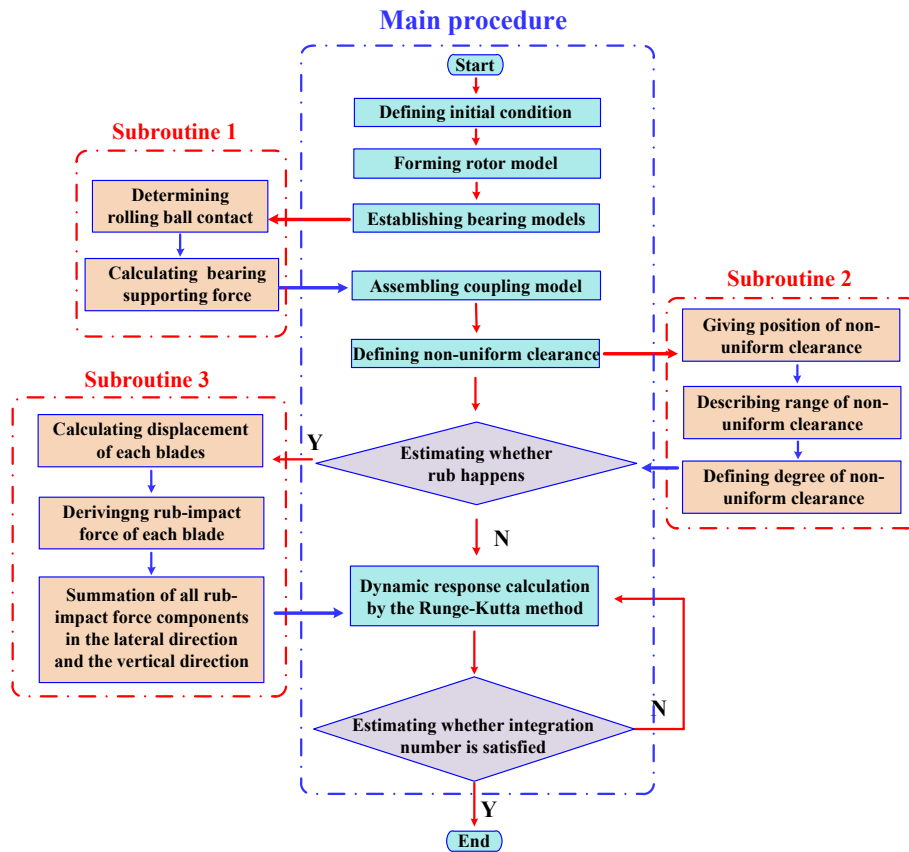
Fig. 12 Flow chart for simulating the dynamic responses of the rotor system with blade-casing rub under non-uniform initial gap.

The time histories of the lateral displacement and angle of twist of the rotor system are presented in the two cases of the uniform and the non-uniform initial gap. By comparing and analysing the difference in responses between the two cases, the influence of non-uniform gap is

deeply studied, which lays down the foundation for the subsequent parametric analysis. According to reference [52], the structural parameters of the rotor system in the simulations are taken and given in Appendix B.

## 3.1 Vibration responses under large initial gap

When the initial gap between blades and casing is large enough, the rub fault can only occur at the non-uniform gap location. To understand the rub characteristics more clearly, the vibration responses of the rotor system under a large initial gap are studied at first. Define the following work condition: $\delta_0=5\times10^{-5}$ m, $\delta_{max}=4.5\times10^{-5}$ m, $\alpha=\dfrac{\pi}{4}$ rad and $\beta=\dfrac{\pi}{9}$ rad. Meanwhile the rotor speed is set to $\omega=200$ rad/s (i.e., 1900 rpm).

Fig. 13 shows the time histories of the lateral displacement and angle of twist of the rotor system under the large uniform initial gap. From Fig. 13(a), it can be seen that the lateral vibration happens around a position which is almost zero, and the vibration amplitude is about 1.91×10^{-5} m, which is smaller than the uniform initial gap. Without rub, the torsional vibration of the rotor system does not occur, as shown in Fig. 13(b).

a) time histories of lateral displacement   b) time histories of angle of twist
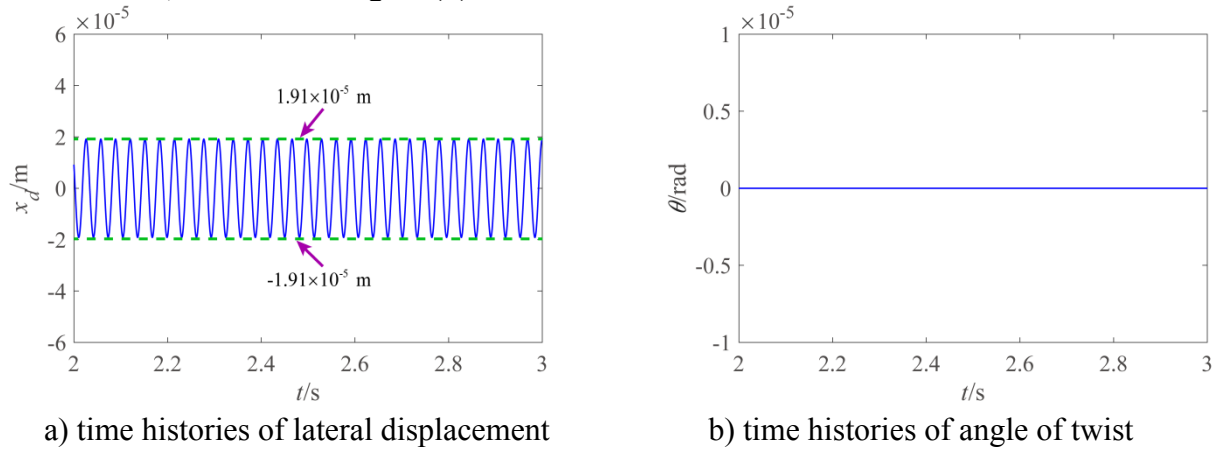
Fig. 13. Vibration responses of the rotor system under a large uniform gap: (a) time histories of lateral displacement and (b) time histories of angle of twist.

Keeping the other parameters constant, then the initial gap is now considered large but non-uniform. Consequently, the time histories of the lateral displacement and angle of twist of the rotor system are given in Fig. 14. Different from that in Fig. 13(a), the vibration in Fig. 14(a) happens around a position which is not zero. Because of the non-uniform gap, the whirling amplitude of the rotor increases to some extent. The time histories of torsion are given in Fig. 14(b) and shown to be periodic.

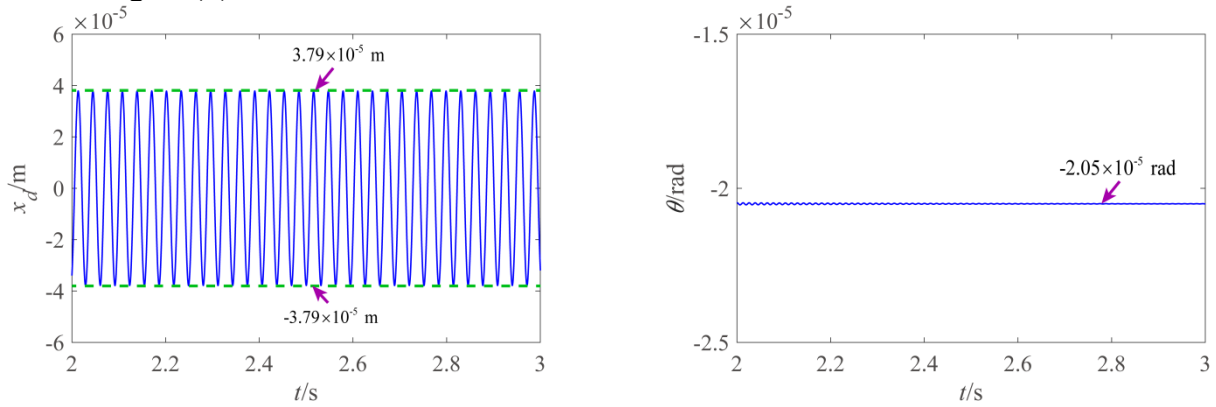a) time histories of lateral displacement   b) time histories of angle of twist
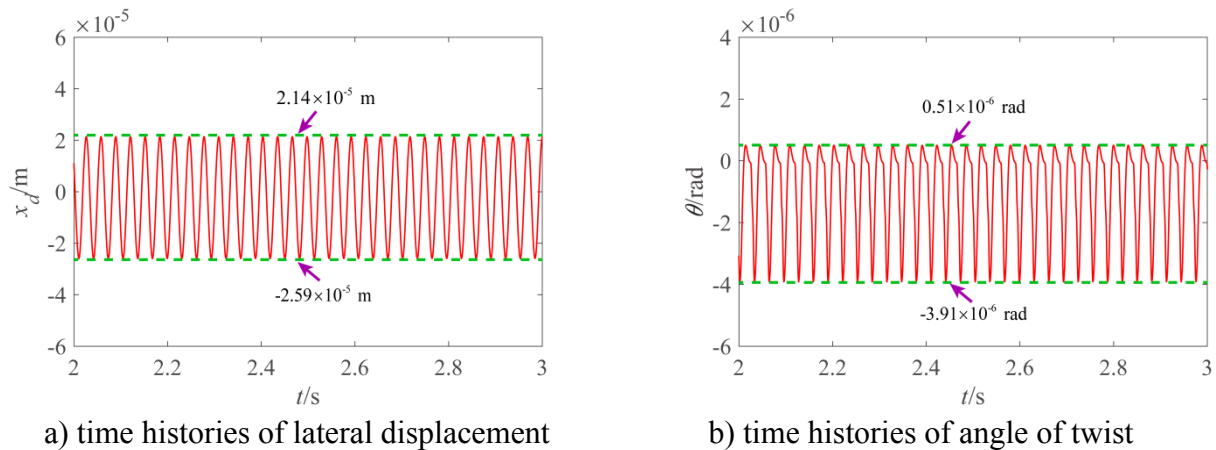
Fig. 14. Vibration responses of the rotor system under a large non-uniform gap: (a) time histories of

lateral displacement and (b) time histories of angle of twist.

3.2 Vibration responses under small initial gap

Next, the vibration of the rotor system under a small initial gap is further discussed. Similar to the previous section, the comparison between dynamic responses under the uniform small gap and the non-uniform small gap is conducted. The so-called small initial gap implies that the rub fault between blades and casing may occur not only at the non-uniform location, but also elsewhere. Compared with the previous studies, this small initial gap, which happens more frequently in aero engines, seems to lead to more complex dynamic behaviour.

Keeping the characteristics of the non-uniform gap (i.e., location α, range β and minimum gap $\delta_0 - \delta_{max}$) unchanged, the initial gap is reset to $\delta_0 = 1.5 \times 10^{-5}$ m. When the small initial gap is uniform, the dynamic responses of the rotor system are depicted in Fig. 15(a). The whirling amplitude of the rotor system is always larger than the uniform small gap, which indicates the occurrence of the full annular rub. In this case, the friction torque M acting on the rotor system remains constant and the resulting angle of twist remains unchanged (i.e., $\theta = -2.05 \times 10^{-5}$ rad), as shown in Fig. 15(b).
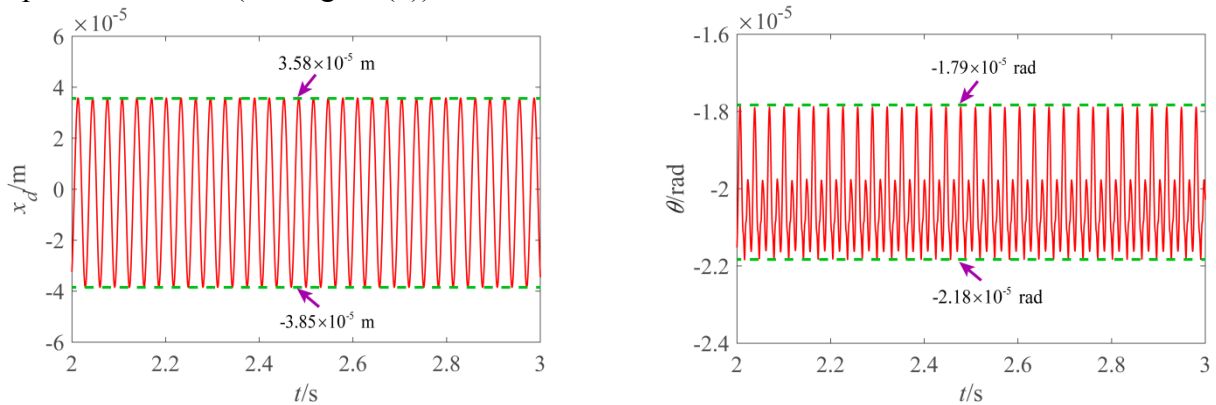

a) time histories of lateral displacement   b) time histories of angle of twist

Fig. 15. Vibration responses of the rotor system under a small uniform gap: (a) time histories of lateral displacement and (b) time histories of angle of twist.

If the initial gap between the blades and casing is small but non-uniform, rub fault will occur at both non-uniform and uniform locations. In contrast, the rub magnitude may be more serious at the non-uniform gap location. As shown in Fig. 16(a), the lateral vibration happens around a position which is not zero. The variation of friction torque caused by the non-uniform gap further leads to the 2T-periodic motion (see Fig. 16(b)).

a) time histories of lateral displacement   b) time histories of angle of twist

Fig. 16. Vibration responses of the rotor system under a small non-uniform gap: (a) time histories of lateral displacement and (b) time histories of angle of twist.
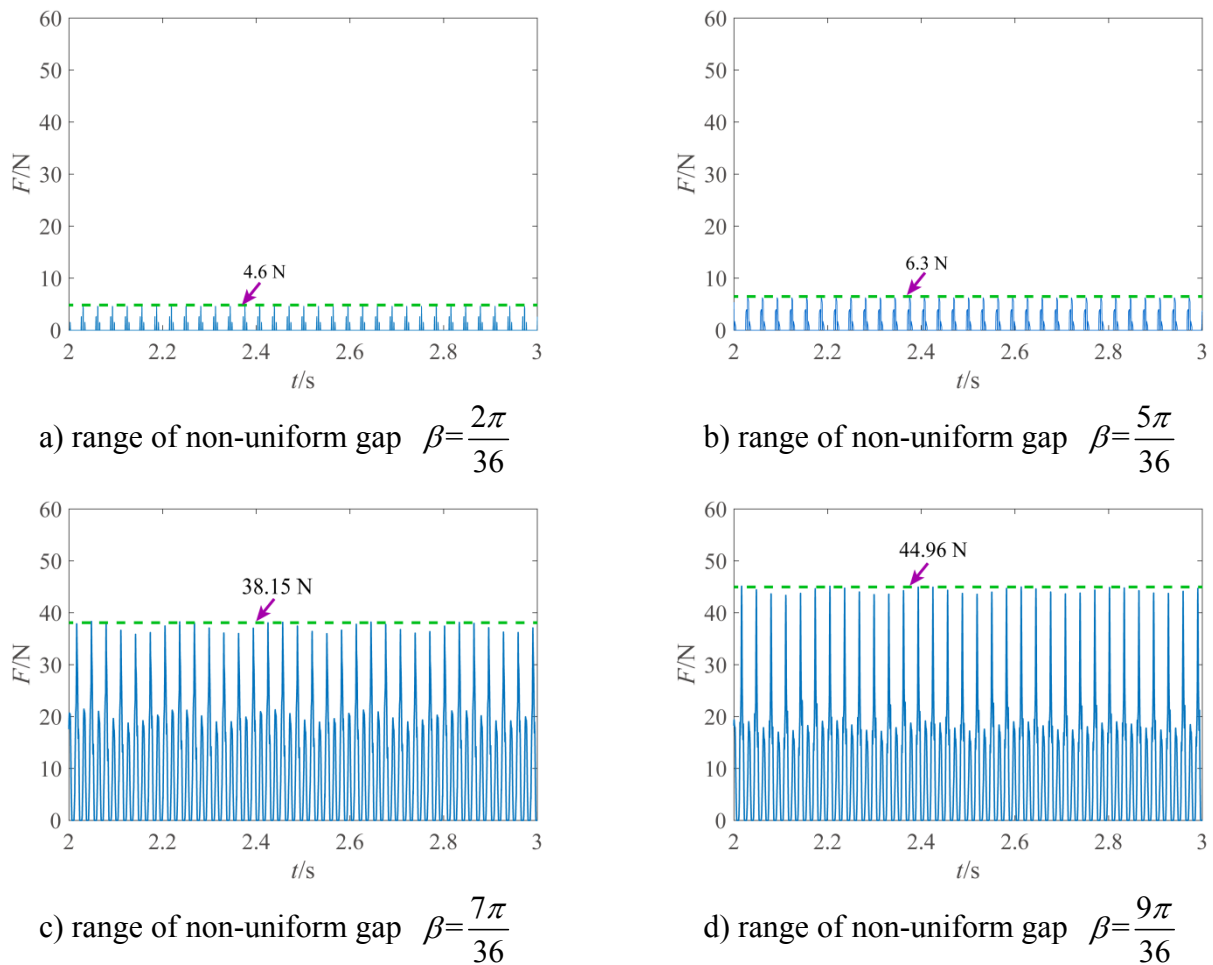
4. Parametric analysis

According to the research given in the previous section, it is known that the vibration responses of the rotor system are more sensitive to the non-uniform gap. Therefore, a parametric analysis of the range of non-uniform gap β, location of the non-uniform gap α and multiple non-uniformities is performed in this section. Through whirl orbits, phase diagrams and frequency spectrums, the dynamic characteristics of the rotor system are investigated in detail. Besides, the variation of the resultant impact force and the resultant impact displacement is discussed as well.

4.1 Effect of range of non-uniform gap

As given in Eq. (22), parameter β plays an important role in describing the non-uniform gap. To directly identify the change of impact magnitude due to this parameter, a large initial gap (i.e., $\delta_0 = 5 \times 10^{-5}$ m) is simulated in this section and then the rub fault only happens at the non-uniform gap location.

Assume the non-uniform gaps occur over $\beta = \left[\dfrac{2\pi}{36}, \dfrac{5\pi}{36}, \dfrac{7\pi}{36}, \dfrac{9\pi}{36} \right]$ rad, respectively, and the rotor speed $\omega = 200$ rad/s remains unchanged. During the rotor operation, the blades mounted on the disc may impact against the casing at the non-uniform gap location. Therefore, it is necessary to calculate the impact forces between these blades and casing at each time instant. These values can be used to evaluate the operation state of the rotor system in advance.

a) range of non-uniform gap $\beta = \dfrac{2\pi}{36}$

b) range of non-uniform gap $\beta = \dfrac{5\pi}{36}$

c) range of non-uniform gap $\beta = \dfrac{7\pi}{36}$

d) range of non-uniform gap $\beta = \dfrac{9\pi}{36}$

Fig. 17. Resultant impact force acting on the rotor system with different non-uniform gap range β

(rad): (a) $\beta=\dfrac{2\pi}{36}$, (b) $\beta=\dfrac{5\pi}{36}$, (c) $\beta=\dfrac{7\pi}{36}$ and (d) $\beta=\dfrac{9\pi}{36}$.

The influences of the range of the non-uniform gap β on the resultant impact force acting on the system are shown in Fig. 17. Since the non-uniform gap only exists in a few local areas, the resultant impact forces appear in the form of discontinuous pluses. In these four cases, with the increase of β, the resultant impact force gradually increases from $F = 4.6\,\text{N}$ to $F = 44.96\,\text{N}$. Meanwhile, the impact times between blades and casing increases significantly. This phenomenon suggests that within a certain range, a wide range of non-uniform gap could aggravate the blade-casing rub and even affect the smooth operation of the rotor system.

a) range of non-uniform gap $\beta=\dfrac{2\pi}{36}$

b) range of non-uniform gap $\beta=\dfrac{5\pi}{36}$

c) range of non-uniform gap $\beta=\dfrac{7\pi}{36}$

d) range of non-uniform gap $\beta=\dfrac{9\pi}{36}$
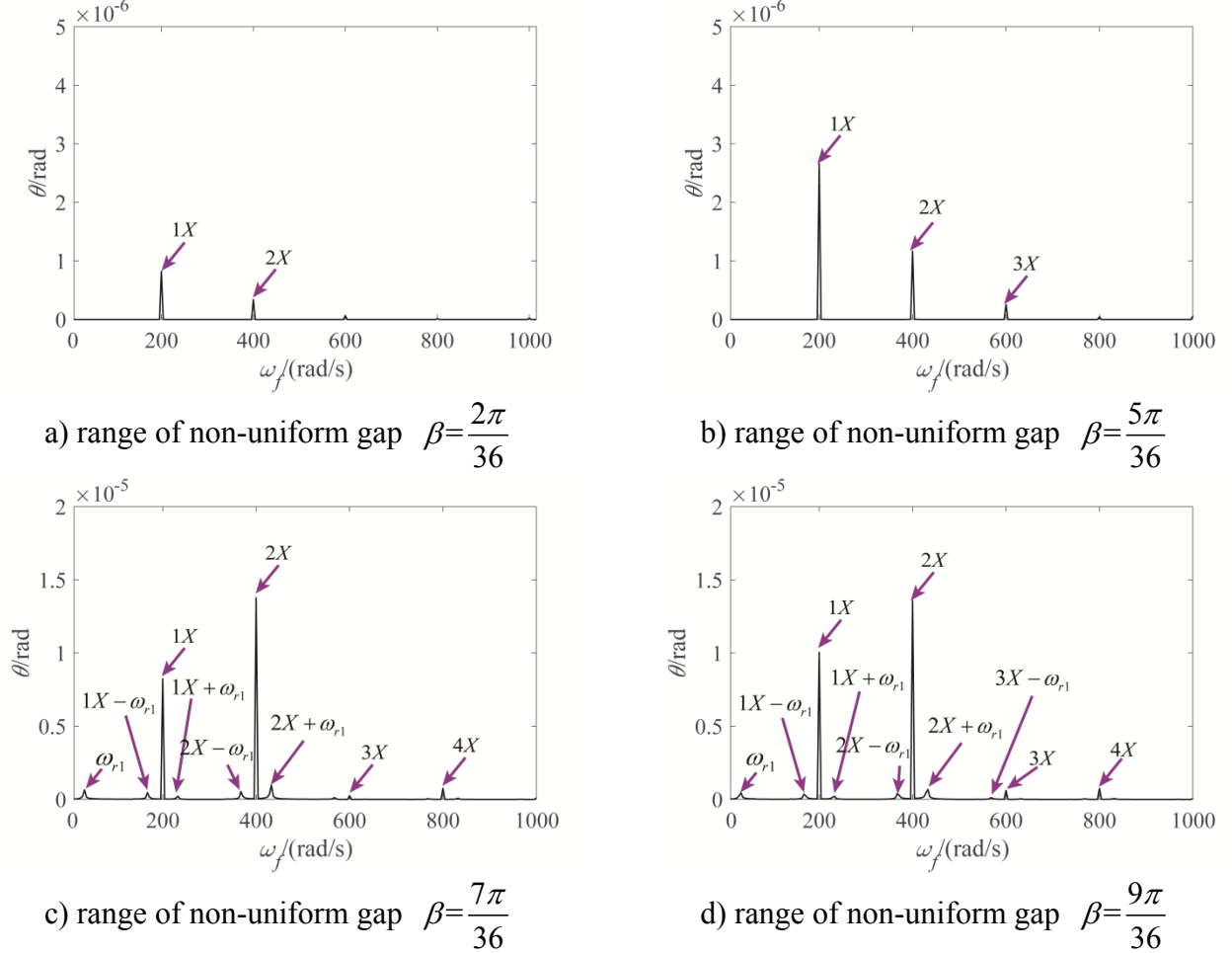
Fig. 18. Frequency spectrums of torsional vibration responses in the above four cases.

In view of the above four cases, the frequency components in the torsional vibration responses are further analysed in terms of their frequency spectrums, as shown in Fig. 18. When the non-uniform range is $\beta=\dfrac{2\pi}{36}\,\text{rad}$, the frequency spectrum includes two components, namely $1X = 200\,\text{rad/s}$ and $2X$. Fig. 18(b) displays the frequency spectrum for $\beta=\dfrac{5\pi}{36}\,\text{rad}$, in which there are three components, namely $1X = 200\,\text{rad/s}$, $2X$ and $3X$. If the non-uniform initial gap becomes more prominent, abundant frequency components appear in the spectrum. For example, Figs. 18(c) and (d) display $1X = 200\,\text{rad/s}$, $2X$, $3X$ and $4X$. In addition, the fault-induced frequency component ω_{r1} and combination resonance frequency components, such as $1X - \omega_{r1}$, $1X + \omega_{r1}$, $2X - \omega_{r1}$, $2X + \omega_{r1}$, are determined.
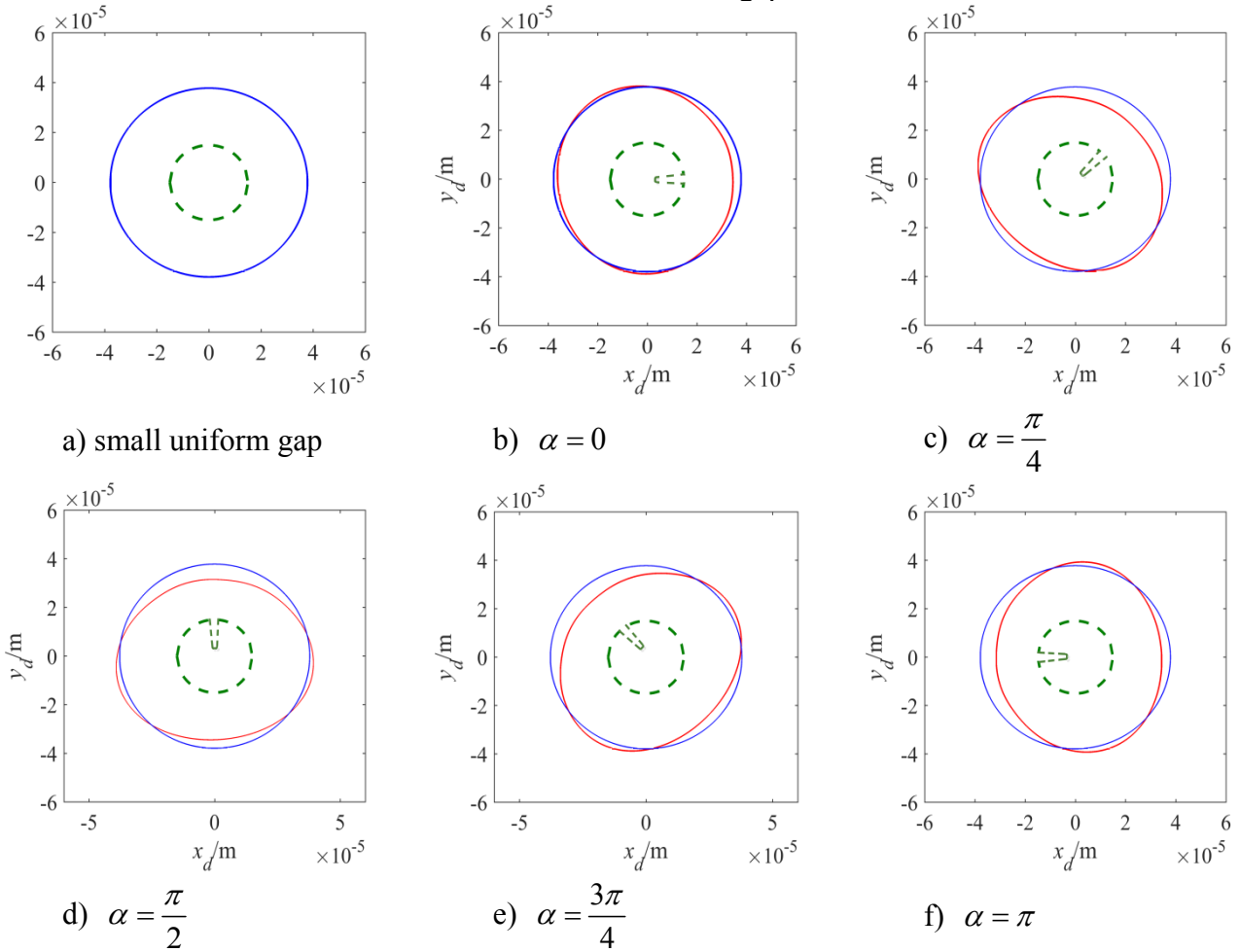
As a result, it could be said that the non-uniform gap range affects the complexity of the torsional motion and leads to rich frequency components.
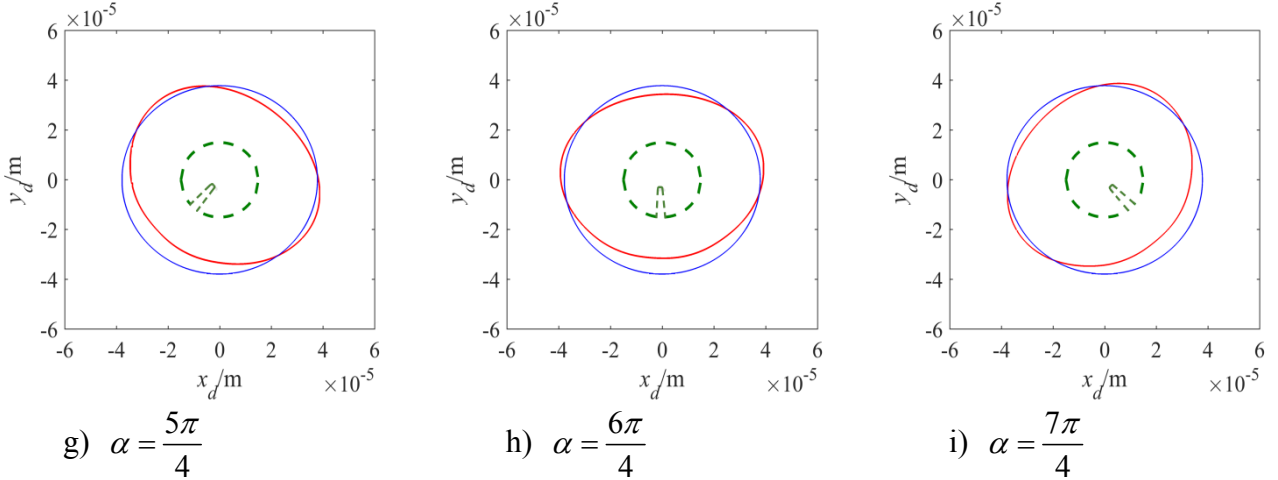
4.2 Effect of location of non-uniform gap

This section focuses on the study of the location of the non-uniform gap by analyzing the variation of whirling orbits. In order to make a proper comparison between rub characteristics under the uniform gap and that under the non-uniform gap, a small initial gap between blades and casing should be considered, namely $\delta_0 = 1.5 \times 10^{-5}$ m.

Keeping the other parameters given in Appendix B unchanged, the location of non-uniform gap is reset to $\alpha = \left[0, \ \dfrac{\pi}{4}, \ \dfrac{\pi}{2}, \ \dfrac{3\pi}{4}, \ \pi, \ \dfrac{5\pi}{4}, \ \dfrac{6\pi}{4}, \ \dfrac{7\pi}{4} \right]$ rad, respectively. In the case of a small uniform gap, the whirling orbits of the rotor system are given in Fig. 19(a), in which the blue line represents the disc whirling orbit and the green dotted line represents the initial gap. Obviously, the whirling orbits appear as a regular circle and the fault form is identified as a full annular rub.

Considering the change of the location of the non-uniform gap α, the evolution of the whirling orbits is shown in Figs. 19(b)-(i), in which the red lines represent the whirling orbits under non-uniform gap and the blue lines represent the whirling orbits under the uniform gap. These plots illustrate that due to the existence of the non-uniform gap, the disc whirling orbit appears as an ellipse instead of a regular circle. More specifically, the direction of the short axis of the ellipse coincides with the direction of the location of non-uniform gap.


a) small uniform gap

b) $\alpha = 0$

c) $\alpha = \dfrac{\pi}{4}$

d) $\alpha = \dfrac{\pi}{2}$

e) $\alpha = \dfrac{3\pi}{4}$

f) $\alpha = \pi$

g) $\alpha = \dfrac{5\pi}{4}$　　　　　　h) $\alpha = \dfrac{6\pi}{4}$　　　　　　i) $\alpha = \dfrac{7\pi}{4}$

Fig. 19. Whirling orbits of the rotor system with different location of non-uniform gap α (rad): (a) small uniform gap, (b) $\alpha = 0$, (c) $\alpha = \dfrac{\pi}{4}$, (d) $\alpha = \dfrac{\pi}{2}$, (e) $\alpha = \dfrac{3\pi}{4}$, (f) $\alpha = \pi$, (g) $\alpha = \dfrac{5\pi}{4}$, (h) $\alpha = \dfrac{6\pi}{4}$ and (i) $\alpha = \dfrac{7\pi}{4}$.

Although all the fault forms shown in Fig. 19 belong to the full annular rub, the rub magnitude under the uniform gap is obviously different from that under the non-uniform gap. The whirling orbits of the rotor system are seen to depend on not only the disc eccentricity, but also the location of non-uniform gap. This feature may provide an efficient way for making fault diagnosis. In other words, sometimes the fault location may be found through analysing the whirling orbits of the rotor system.

4.3 Effect of non-uniform gaps at multiple locations

In the previous sub-sections where the influences of the non-uniform gap have been investigated, the gap occurs at only one location. In real aero-engines, non-uniform gaps are likely to appear at multiple locations, whose influences are the topic of this sub-section.

Fig. 20 displays three scenarios of the initial gap between blades and casing, including a uniform gap, one non-uniform gap at $\alpha = \dfrac{\pi}{4}$ rad, and two non-uniform gaps at $\alpha = \dfrac{\pi}{4}$ rad and $\alpha = \dfrac{5\pi}{4}$ rad.

a) a uniform gap　　　　　　b) one non-uniform gap　　　　　　c) two non-uniform gaps
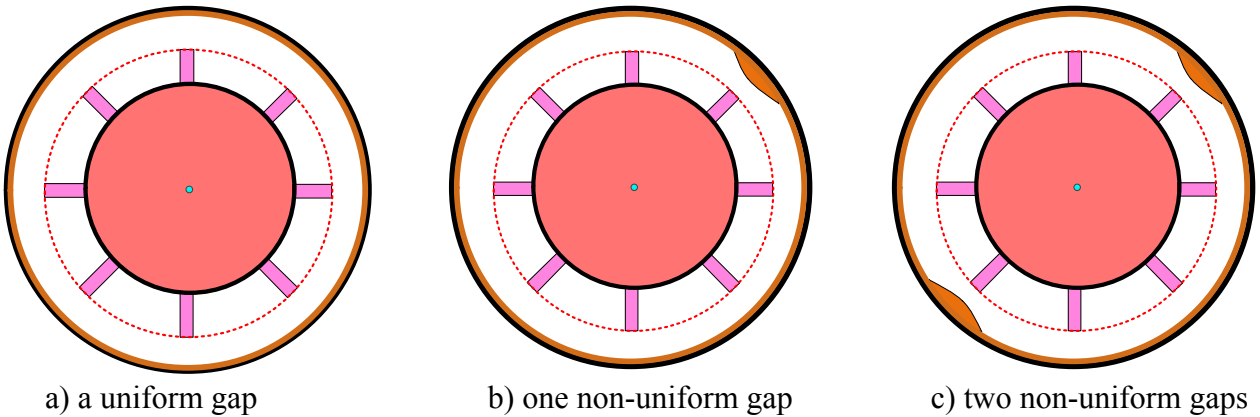
Fig. 20. Schematic diagram for three scenarios of rotor-casing system: (a) with a uniform gap, (b) with one non-uniform gap, and (c) with two non-uniform gaps.

For these three cases of initial gaps, the rub-impact features between rotating blades and casing

are computed, in which Fig. 21(a) displays the variation of the maximum resultant impact displacement and Fig. 21(b) gives the variation of the maximum resultant impact force. Within the frequency interval of $\omega = [100, 500]$ rad/s, the most serious rub-impact appears at $\omega = 250$ rad/s.

The impact displacement and the resultant impact force are mainly determined by the disc motion. When the rotational speed is close to the critical speed of the system, the disc motion becomes large and the corresponding rub-impact becomes more serious. When the rotational speed exceeds the critical speed and moves away from it, the rub-impact becomes slight. Therefore, the trends shown in Fig. 21 are indeed due to the resonance of the rotor system. What is more, the resultant impact displacement shown in Fig. 20(c) is larger than those shown in Figs. 20(a) and (b). Meanwhile, the similar trend applies to the maximum resultant impact force (see Fig. 21(b)).

When the rotor speed is smaller than the resonance speed, the blade-casing rub under the uniform gap will gradually become more serious with the increase of the motor speed. However, when the motor speed is larger than the resonance speed, the rub will gradually ease with the increase of the rotor speed. And it can even completely disappear until the rotor speed reaches $\omega = 350$ rad/s. If the non-uniform gap exists in one or two locations, the blade-casing rub will continue to happen within this speed range.

a) maximum resultant impact displacement

b) maximum resultant impact force
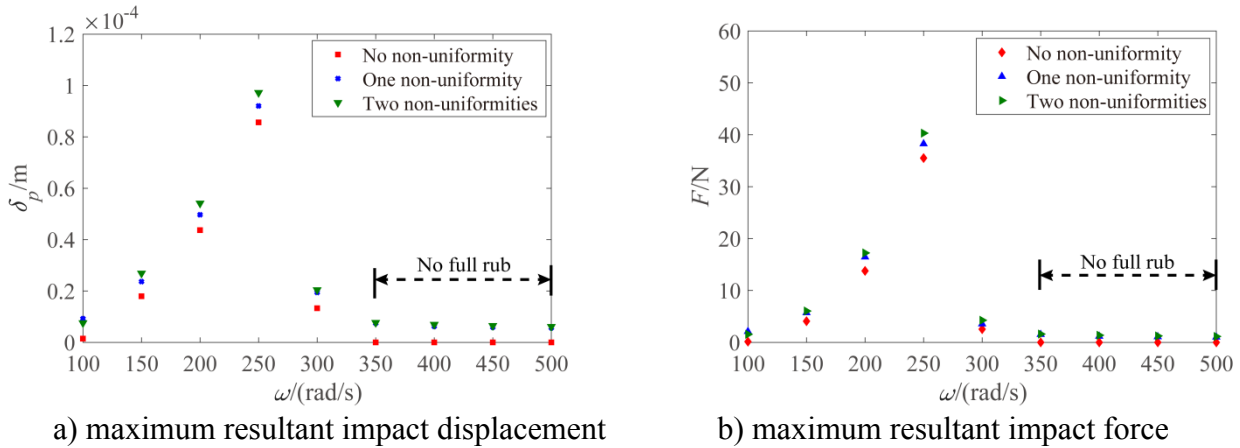
Fig. 21. Within the speed interval of $\omega = [100, 500]$ rad/s, variation of impact degree in the above three cases: (a) maximum resultant impact displacement and (b) maximum resultant impact force.

The results indicate that from the viewpoint of impact force and impact displacement, the non-uniform gaps at two locations may present the greatest hazard, which may affect the operation quality of the rotor system more seriously.

In the following part, the spatial distribution of the two non-uniform gaps and its influence on the rotor vibration characteristics are studied. For the sake of analysis, a variable α_r is introduced to describe the relative location between two non-uniform gaps. Let the location of the first one be α and then that of the second one be $\alpha + \alpha_r$.

Fig. 22 displays the spatial distribution of two non-uniform gaps, in 17 scenarios over a full circle of four quadrants. Therefore, the two variables describing the spatial distribution are defined as

$$\begin{cases} \alpha = 0 \text{ rad,} \\ \alpha_r = [1, 2, 3, 4, 5, 6, 7, 8, 9, 10, 11, 12, 13, 14, 15, 16, 17] \times \dfrac{\pi}{9} \text{ rad.} \end{cases} \tag{33}$$

When the rotor speed is $\omega = 200$ rad/s and the initial gap is $\delta_0 = 1.5 \times 10^{-5}$ m, the maximum lateral displacement and the maximum vertical displacement of the disc can be further obtained in the 17 cases of the above spatial distributions of initial gaps. Fig. 23(a) shows that in quadrants (I) and (III), the lateral displacement of the disc gradually develops with the increase of α_r.

Nevertheless, it decreases obviously with the increase of α_r in quadrants (II) and (IV). Under the spatial distributions shown in Fig. 22, the variation of the vertical displacement is also given in Fig. 23(b). The reduction of the vertical displacement is observed in quadrants (I) and (III). In contrast, an increasing trend of the vertical displacement is revealed in quadrants (II) and (IV).

Overall, the spatial distributions of two non-uniform gaps can directly affect the whirling amplitude of the rotor system. When the effect of the non-uniform gap on the rotor dynamics is evaluated, the gap distribution is also one of the important aspects, which should be paid enough attention to.
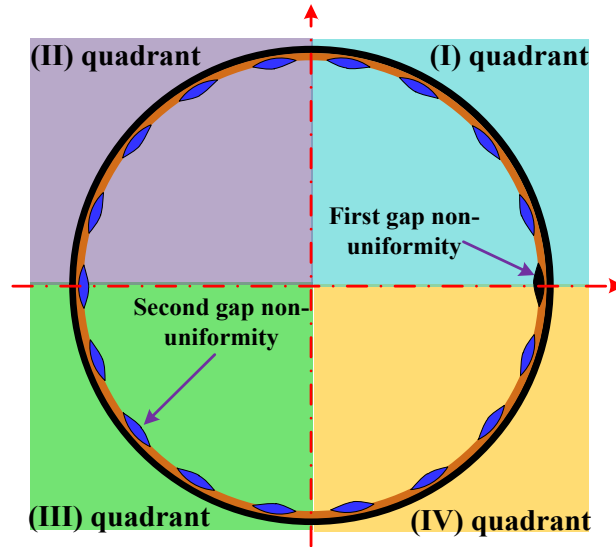
**Fig. 22.** Diagram of spatial distributions of two non-uniform gaps.

a) maximum lateral displacement $x_{d,\max}$ b) maximum vertical displacement $y_{d,\max}$
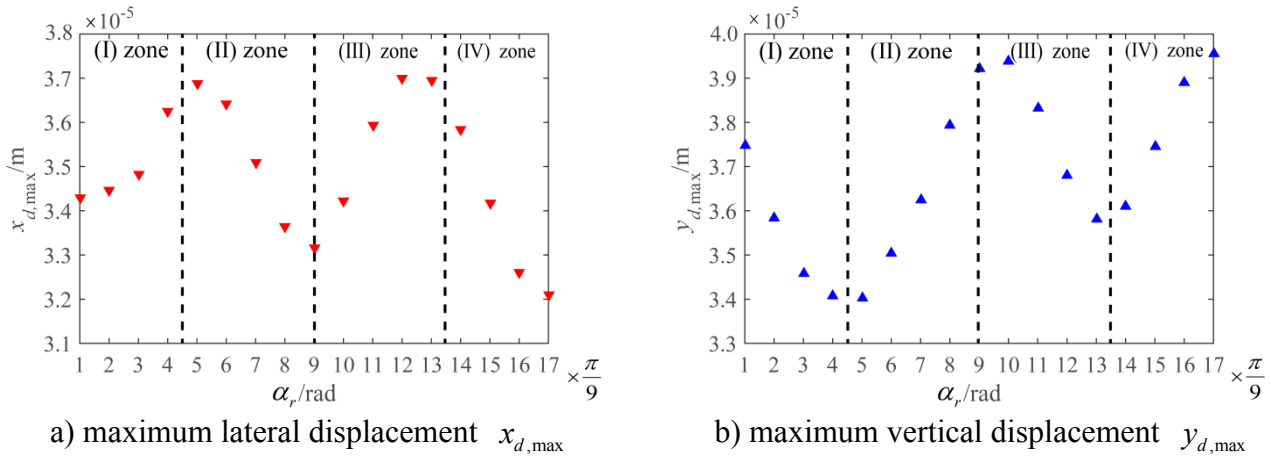
Fig. 23. Effect of relative location α_r on the vibration responses of the disc: (a) maximum lateral displacement $x_{d,\max}$ and (b) maximum vertical displacement $y_{d,\max}$.

At last, the more complicated situations of asymmetric spatial distributions of non-uniform gaps are considered. As shown in Fig. 24, the non-uniform gaps appear at four locations, and they are $\alpha_1 = \dfrac{\pi}{4}$ rad, $\alpha_2 = \dfrac{3\pi}{4}$ rad, $\alpha_3 = \dfrac{5\pi}{4}$ rad and $\alpha_4 = \dfrac{7\pi}{4}$ rad.

A completely symmetric case is shown in Fig. 24(a), in which the ranges of non-uniform gap at four locations are set to $\beta_1 = \beta_2 = \beta_3 = \beta_4 = \dfrac{\pi}{9}$ rad and the magnitude of the non-uniform gap at the

four locations are set to $\delta_{max,1} = \delta_{max,2} = \delta_{max,3} = \delta_{max,4} = 1 \times 10^{-5}$ m. For comparison, the asymmetric case of having a different range at location 1 (i.e., $\beta_1 = \dfrac{\pi}{18}$ rad) is shown in Fig. 24(b). In addition, Fig. 24(c) displays another asymmetric case, in which the magnitude of the non-uniform gap at location 1 is different from those at other locations, namely $\delta_{max,1} = 0.5 \times 10^{-5}$ m.

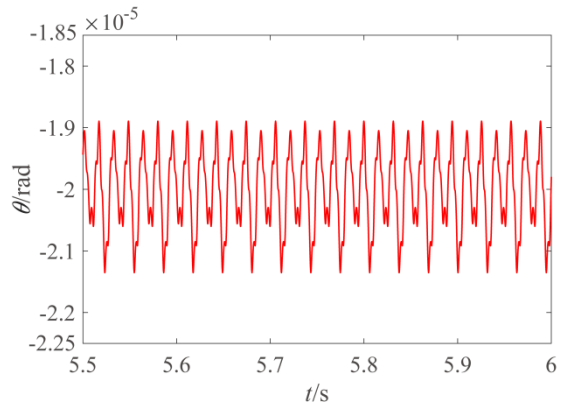a) symmetric case   b) asymmetric case   c) asymmetric case
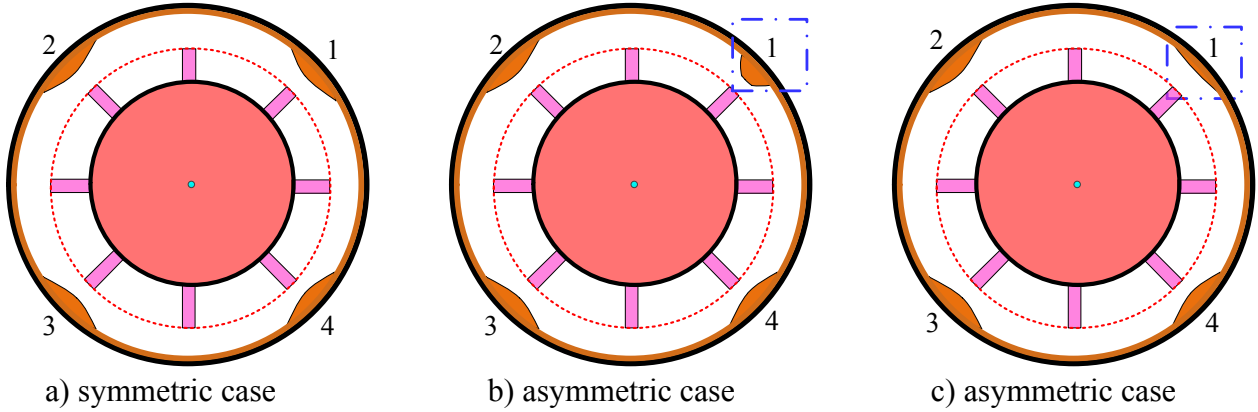
Fig. 24. Schematic diagram of the non-uniform gaps at four locations: (a) symmetric case, (b) asymmetric case of having a different range of non-uniform gap at location 1, and (c) asymmetric case of having a different magnitude of non-uniform gap at location 1.

In discussion of these three cases, the phase diagrams and the time histories of torsional vibration of the rotor system at $\omega = 200$ rad/s are shown in Fig. 25. Under the symmetric distribution of the non-uniform gaps, the system responses include a regular $2T$-periodic motion, as shown in Figs. 25(a) and (b).

a) phase diagram of torsional vibration   b) time histories of torsional vibration

c) phase diagram of torsional vibration   d) time histories of torsional vibration
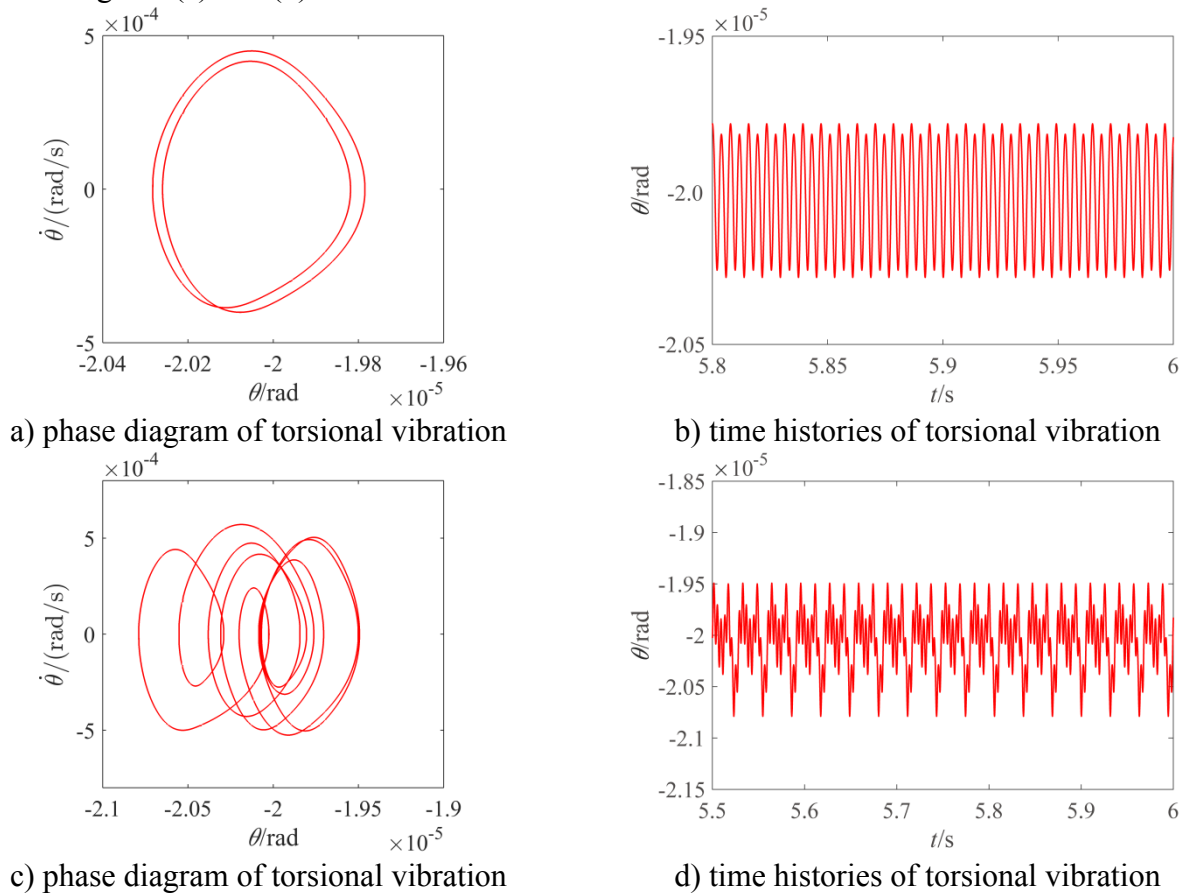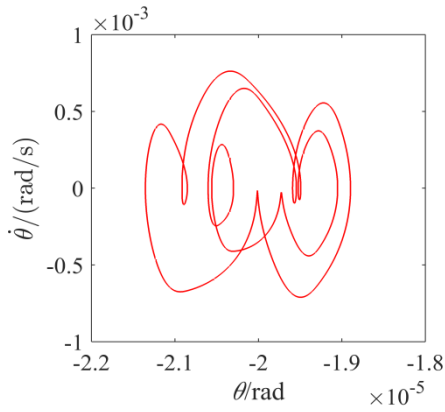
e) phase diagram of torsional vibration   f) time histories of torsional vibration

Fig. 25. Phase diagrams and time histories of torsional vibration of the rotor system in the above three cases: (a) and (b) symmetric case shown in Fig. 24(a), (c) and (d) asymmetric case shown in Fig. 24(b), (e) and (f) asymmetric case shown in Fig. 24(c).

However, if symmetry is lost, the system responses will change obviously. For example, complicated dynamic phenomena appear in Figs. 25(c)-(f), and the amplitudes of the torsional vibration are amplified by the asymmetry. Based on the comparative analysis, it is evident that when there are multiple non-uniform gaps between blades and casing, an asymmetric gap distribution can have a more detrimental effect on the stability of the rotor system.

5. Conclusions

Due to aerodynamic loads, thermal loads, blade coating inhomogeneity and casing deformation, the initial gap between the blades and the casing of an aero engine may be non-uniform rather than ideally uniform. In order to predict the influence of blade-casing rub under a non-uniform gap on the normal operation of rotating machines, a dynamic model of rolling bearings-rotor system with blades is presented in this paper. By comparing the vibration responses of the system under a non-uniform gap with those under a uniform gap, the potential dynamic problems caused by the non-uniform gap are revealed. Moreover, a parametric analysis of various influential system factors is conducted. Some conclusions are summarized as follows:

(1) A blade-casing impact experiment performed on a rotor test rig confirms that the Lankarani-Nikravesh model is suitable for describing the impact mechanism in the case of a non-uniform initial gap.

(2) Compared with the case of a uniform gap, a non-uniform initial gap could lead to rich vibration phenomena in the dynamic responses, especially in the torsional responses. Due to the non-uniform gap, the vibration of the rotor system happens around a position which is not zero.

(3) Within a certain range, increasing the non-uniform gap range will increase the motion complexity, and also aggravate the rub severity between blades and casing. This means that a wider non-uniform range is easier to affect the smooth operation of rotating machines.

(4) The whirling orbits of the rotor system are affected by not only the disc eccentricity, but also the location of the non-uniform gaps. From the viewpoint of fault diagnosis, fault location may be identified through analysing the whirling orbits.

(5) In the presence of non-uniform gaps at multiple locations, the rub severity between blades and casing tends to get worse, including a greater impact force and impact displacement. In addition, an asymmetric spatial distribution of non-uniform gaps has a more detrimental effect on stability of the rotor system.

Acknowledgements

Appendix A

To obtain the bending-torsional coupled vibration equations of the rotational disc, the partial derivative terms in the Lagrange's method are respectively expressed as

$$
\begin{cases}
\dfrac{d}{dt}\left(\dfrac{\partial T}{\partial \dot{x}_d}\right) = m_d \ddot{x}_d + m_e \ddot{x}_d - m_e e \dot{\varphi}_d^2 \cos\varphi_d - m_e e \ddot{\varphi}_d \sin\varphi_d, \\[2mm]
\dfrac{\partial D}{\partial \dot{x}_d} = 2c_b \dot{x}_d - c_b \dot{x}_{ls} - c_b \dot{x}_{rs}, \\[2mm]
\dfrac{\partial V}{\partial x_d} = 2k_b x_d - k_b x_{ls} - k_b x_{rs},
\end{cases}
\tag{A1}
$$

$$
\begin{cases}
\dfrac{d}{dt}\left(\dfrac{\partial T}{\partial \dot{y}_d}\right) = m_d \ddot{y}_d + m_e \ddot{y}_d - m_e e \dot{\varphi}_d^2 \sin\varphi_d + m_e e \ddot{\varphi}_d \cos\varphi_d, \\[2mm]
\dfrac{\partial D}{\partial \dot{y}_d} = 2c_b \dot{y}_d - c_b \dot{y}_{ls} - c_b \dot{y}_{rs}, \\[2mm]
\dfrac{\partial V}{\partial y_d} = 2k_b y_d - k_b y_{ls} - k_b y_{rs},
\end{cases}
\tag{A2}
$$

and

$$
\begin{cases}
\dfrac{d}{dt}\left(\dfrac{\partial T}{\partial \dot{\theta}}\right) = \left(J_0 + m_e e^2\right)\ddot{\varphi}_d - m_e e \sin\varphi_d \ddot{x}_d + m_e e \cos\varphi_d \ddot{y}_d \\[2mm]
\qquad\qquad\qquad - m_e e \dot{\varphi}_d \cos\varphi_d \dot{x}_d - m_e e \dot{\varphi}_d \sin\varphi_d \dot{y}_d, \\[2mm]
\dfrac{\partial D}{\partial \dot{\theta}} = c_t \dot{\theta}, \\[2mm]
\dfrac{\partial V}{\partial \theta} = k_t \theta.
\end{cases}
\tag{A3}
$$

For deriving the equation for the vibration of the left supporting pedestals, the terms used in the Lagrange's equations are

$$
\begin{cases}
\dfrac{d}{dt}\left(\dfrac{\partial T}{\partial \dot{x}_{ls}}\right) = m_{ls}\ddot{x}_{ls}, \\[2mm]
\dfrac{\partial D}{\partial \dot{x}_{ls}} = c_b \dot{x}_{ls} - c_b \dot{x}_d, \\[2mm]
\dfrac{\partial V}{\partial x_{ls}} = k_b x_{ls} - k_b x_d,
\end{cases}
\quad \text{and} \quad
\begin{cases}
\dfrac{d}{dt}\left(\dfrac{\partial T}{\partial \dot{y}_{ls}}\right) = m_{ls}\ddot{y}_{ls}, \\[2mm]
\dfrac{\partial D}{\partial \dot{y}_{ls}} = c_b \dot{y}_{ls} - c_b \dot{y}_d, \\[2mm]
\dfrac{\partial V}{\partial y_{ls}} = k_b y_{ls} - k_b y_d.
\end{cases}
\tag{A4}
$$

Similarly, during the derivation process of the right pedestal vibration, the terms used in the Lagrange's equations are given by

$$\begin{cases} \dfrac{d}{dt}\left(\dfrac{\partial T}{\partial \dot{x}_{rs}}\right) = m_{rs}\ddot{x}_{rs}, \\[3mm] \dfrac{\partial D}{\partial \dot{x}_{rs}} = c_b \dot{x}_{rs} - c_b \dot{x}_d, \\[3mm] \dfrac{\partial V}{\partial x_{rs}} = k_b x_{rs} - k_b x_d. \end{cases} \text{and} \begin{cases} \dfrac{d}{dt}\left(\dfrac{\partial T}{\partial \dot{y}_{rs}}\right) = m_{rs}\ddot{y}_{rs}, \\[3mm] \dfrac{\partial D}{\partial \dot{y}_{rs}} = c_b \dot{y}_{rs} - c_b \dot{y}_d, \\[3mm] \dfrac{\partial V}{\partial y_{rs}} = k_b y_{rs} - k_b y_d. \end{cases} \quad (A5)$$

Appendix B

Table 1 Main parameters of a rotor-bearing-system with blades [52]

Physical parameter	Variable	Value
Equivalent mass of disc with blades (kg)	m_d	8.75
Eccentric mass of disc (kg)	m_e	2.19
Disc radius (m)	R_d	0.1725
Disc mass moment of inertia (kg.m^2)	J_0	0.1302
Left and right pedestal mass (kg)	m_{ls} , m_{rs}	4.375
Lateral bending stiffness (MN/m)	k_b	0.15
Torsional stiffness (N.m/rad)	k_t	13913
Lateral bending damping (N.s/m)	c_b	149.99
Torsional damping (N.s/rad)	c_t	45.68
Unbalance eccentricity (mm)	e	0.0572
Impact stiffness (MN/m)	k_p	75
Coefficient of restitution	c_e	0.96
Contact stiffness of rolling ball (MN/m)	C_b	133.4
Initial clearance of rolling bearing (mm)	r_0	0.004
Rolling ball number	N_r	16
Rotating blade number	N	8
Rotating blade length (m)	l_b	0.086

Conflict of interest

We declare that we do not have any commercial or associative interest that represents a conflict of interest in connection with the work submitted.

References

[1] M. Behzad, M. Alvandi, Unbalance-induced rub between rotor and compliant-segmented stator. J. Sound Vib. 429 (2018): 96-129.

[2] S.K. Sinha, Non-linear dynamic response of a rotating radial Timoshenko beam with periodic pulse loading at the free-end. Int. J. Non Linear Mech. 40(1) (2005): 113-149.

[3] R.E. Chupp, R.C. Hendricks, S.B. Lattime, B.M. Steinetz, Sealing in turbomachinery. J. Propul. Power. 22 (2006): 313-349.

[4] G. Jacquet-Richardet, M. Torkhani, P. Cartraud, Rotor to stator contacts in turbomachines. Review and application. Mech. Syst. Signal Process. 40 (2013): 401-420.

[5] T.H. Patel, A.K. Darpe, Study of coast-up vibration response for rub detection. Mech. Mach. Theory. 44(8) (2009) 1570-1579.

[6] G. Chen, A new rotor-ball bearing-stator coupling dynamics model for whole aero-engine

vibration. J. Vib. Acoust. 131(6) (2009): 061009-1-061009-9.

[7]   Z. Huang, J. Zhou, M. Yang, Vibration characteristics of a hydraulic generator unit rotor system with parallel misalignment and rub-impact. Arch. Appl. Mech. 81 (2011): 829-838.

[8]   B. Schweizer, Oil whirl, oil whip and whirl/whip synchronization occurring in rotor system with full-floating ring bearings. Nonlin. Dyn. 57 (2009): 509-532.

[9]   A.J. Hu, L. Xiang, Y. Zhang, Experimental study on the intrawave frequency modulation characteristic of rotor rub and crack fault. Mech. Syst. Signal Process. 118 (2019): 209-225.

[10] A. Muszynska, P. Goldman, Chaotic responses of unbalanced rotor/bearing/stator systems with looseness or rubs. Chaos. Soltions & Fractals. 5(9) (1995): 1683-1704.

[11] H. Ma, F.L. Yin, Y.Z. Guo, X.Y. Tai, B.C. Wen, A review on dynamic characteristics of blade-casing rubbing. Nonlin. Dyn. 84 (2016): 437-472.

[12] A. Muszynska, Rotor-to-stationary element rub-related vibration phenomena in rotating machinery literature survey. Shock Vib. Dig. 21 (1989): 3-11.

[13] J. Jiang, Determination of the global responses characteristics of a piecewise smooth dynamical system with contact. Nonlin. Dyn. 57 (2009): 351-361.

[14] F. Chu, Z. Zhang, Bifurcation and chaos in a rub-impact Jeffcott rotor system. J. Sound Vib. 210(1) (1998): 1-18.

[15] J.Y. Cao, C.B. Ma, Z.D. Jiang, S.G. Liu, Nonlinear dynamic analysis of fractional order rub-impact rotor system. Commun. Nonlinear Sci. Numer. Simul. 16 (2011): 1443-1463.

[16] J. Hong, P.C. Yu, D.Y. Zhang, Z.C. Liang, Modal characteristics analysis for a flexible rotor with non-smooth constraint due to intermittent rub-impact. Chinese. J. Aeronaut. 31(3) (2018): 498-513.

[17] A. Zilli, R.J. Williams, D.J. Ewins, Nonlinear Dynamics of a simplified model of an overhung rotor subjected to intermittent annular rubs. J. Eng. Gas Turbines Power. 137(6) (2015): 065001-1-065001-10.

[18] H.B. Zhang, Y.S. Chen, J. Li, Bifurcation on synchronous full annular rub of rigid-rotor elastic-support system. Appl. Math. Mech. –Engl. Ed., 33(7) (2012): 865-880.

[19] Y.H. Chen, G. Yao, J. Jiang, The forward and the backward full annular rubbing dynamics of a coupled rotor-casing/foundation system. Int. J. Dynam. Control. 1 (2013): 116-128.

[20] C-C. Fan, J-W. Syu, M-C. Pan, W-C. Tsao, Study of start-up vibration response for oil whirl, oil whip and dry whip. Mech. Syst. Signal Process. 25 (2011): 3102-3115.

[21] Y. Yang, D.Q. Cao, D.Y. Wang, G.Y. Jiang, Fixed-point rubbing characteristic analysis of a dual-rotor system based on the Lankarani-Nikravesh model. Mech. Mach. Theory. 103 (2016): 202-221.

[22] Y. Yang, D.Q. Cao, T.H. Yu, D.Y. Wang, C.G. Li, Prediction of dynamic characteristics of a dual-rotor system with fixed point rubbing—Theoretical analysis and experimental study. Int. J. Mech. Sci. 115-116 (2016): 253-261.

[23] C.Z. Sun, Y.S. Chen, L. Hou, Steady-state response characteristics of a dual-rotor system induced by rub-impact. Nonlin. Dyn. 86 (2016): 91-105.

[24] M. Guskov, J.J. Sinou, F. Thouverez, O.S. Naraikin, Experimental and numerical investigations of a dual-shaft test rig with intershaft bearing. Int. J. Rotat. Mach. 128(2) (2007): 308-321.

[25] N.F. Wang, D.X. Jiang, K. Behdinan, Vibration response analysis of rubbing faults on a dual-rotor bearing system. Arch. Appl. Mech. 87 (2017): 1891-1907.

[26] A. Millecamps, A. Batailly, M. Legrand, et al., Snecma's viewpoint on the numerical and experimental simulation of blade-tip/casing unilateral contacts. In: ASME Turbo Expo 2015: Turbine Technical Conference and Exposition, American Society of Mechanical Engineers (2015).

[27] H. Ma, F.L. Yin, Z.Y. Wu, X.Y. Tai, B.C. Wen, Nonlinear vibration response analysis of a rotor-blade system with blade-tip rubbing. Nonlin. Dyn. 84 (2016): 1225-1258.

[28] C. Padova, J. Barton, M.G. Dunn, S. Manwaring, Experimental results from controlled blade

tip/shroud rubs at engine speed. J. Turbomach. 129 (2007): 713-723.

[29] S.K. Sinha, Dynamic characteristics of a flexible bladed-rotor with Coulomb damping due to tip-rub. J. Sound Vib. 273 (2004): 875-919.

[30] N.F. Wang, C. Liu, D.X. Jiang, K. Behdinan, Casing vibration response prediction of dual-rotor-blade-casing system with blade-casing rubbing. Mech. Syst. Signal Process. 118 (2019): 61-77.

[31] B.Q. Li, H. Ma, J. Zeng, X.M. Guo, B.C. Wen, Rotating blade-casing rubbing simulation considering casing flexibility. Int. J. Mech. Sci. 148 (2018): 118-134.

[32] N. Lesaffre, J.-J. Sinou, F. Thouverez, Contact analysis of a flexible bladed-rotor. Eur. J. Mech. A-Solids. 26 (2007) 541-557.

[33] S. Bab, S.E. Khadem, M. Shahgholi, A. Abbasi, Vibration attenuation of a continuous rotor-blisk-journal bearing system employing smooth nonlinear energy sinks. Mech. Syst. Signal Process. 84 (2017): 128-157.

[34] S. Bab, M. Najafi, J.F. Sola, A. Abbasi, Annihilation of non-stationary vibration of a gas turbine rotor system under rub-impact effect using a nonlinear absorber. Mech. Mach. Theory. 139 (2019): 379-406.

[35] Z.Y. Qin, X.J. Pang, B. Safaei, F.L. Chu, Free vibration analysis of rotating functionally graded CNT reinforced composite cylindrical shells with arbitrary boundary conditions. Compos. Struct. 220 (2019): 847-860.

[36] Z.Y. Qin, Z.B. Yang, J. Zu, F.L. Chu, Free vibration analysis of rotating cylindrical shells coupled with moderately thick annular plate. Int. J. Mech. Sci. 142-143 (2018) 127-139.

[37] Z.Y. Qin, F.L. Chu, J. Zu, Free vibrations of cylindrical shells with arbitrary boundary conditions: a comparison study. Int. J. Mech. Sci. 133 (2017) 91-99.

[38] P. Varney, I. Green, Rotordynamic analysis using the complex transfer matrix: an application to elastomer supports using the viscoelastic correspondence principle. J. Sound Vib. 333 (2014) 6258-6272.

[39] A. Tatar, C.W. Schwingshackl, M.I. Friswell, Dynamic behaviour of three-dimensional planetary geared rotor systems. Mech. Mach. Theory. 134 (2019) 39-56.

[40] D. Heller, I. Sever, C.W. Schwingshackl, Vibration analysis from simulated tip timing sensor signal shape modulation. Proceedings of ASME Turbo Expo 2018: Turbomachinery Technical Conference and Exposition 11-15 July 2018, Oslo, Norway.

[41] M.I. Friswell, J.E.T. Penny, S.D. Garvey, A.W. Lees, Dynamics of Rotating Machines, Cambridge University Press, 2010.

[42] C. Villa, J.-J. Sinou, F. Thouverez, Stability and vibration analysis of a complex flexible rotor bearing system. Commun. Nonlinear Sci. Numer. Simul. 13 (2008) 804-821.

[43] T.A. Harris, M.N. Kotzalas, Essential concepts of bearing technology, CRC press Boca Raton, 2006

[44] E.E. Halila, D.T. Lenahan, T.T. Thomas, Energy efficient engine, high pressure turbine test hardware detailed design report. NASA CR-167955 (1982).

[45] T.N. Rhys-Jones, Thermal sprayed coating systems for surface protection and clearance control applications in aero engines, Surf. Coat. Technol. 43/44 (1990): 402-415.

[46] S.B. Lattime, B.M. Steinetz, Turbine engine clearance control systems: current practices and future directions. 38th AIAA/ASME/SAE/ASEE Joint Propulsion Conference & Exhibit 7-10 July 2002, Indianapolis, Indiana.

[47] U. Ehehalt, O. Alber, R. Markert, G. Wegener, Experimental observations on rotor-to-stator contact. J. Sound Vib. 446 (2019) 453-467.

[48] P. Zhou, M.G. Du, S.Q. Chen, Q.B. He, Z.K. Peng, W.M. Zhang, Study on intra-wave frequency modulation phenomenon in detection of rub-impact fault. Mech. Syst. Signal Process. 122 (2019): 342-363.

[49] P. Varney, I. Green, Nonlinear phenomena, bifurcations, and routes to chaos in an

asymmetrically supported rotor-stator contact system. J. Sound Vib. 336 (2015) 207-226.

[50] N. Vlajic, A.R. Champneys, B. Balachandran, Nonlinear dynamics of a Jeffcott rotor with torsional deformations and rotor-stator contact. Int. J. Non-Linear Mech. 92 (2017) 102-110.

[51] G. Chen, Simulation of casing vibration resulting from blade-casing rubbing and its verifications. J. Sound Vib. 361 (2016) 190-209.

[52] T.H. Patel, M.J. Zuo, X.M. Zhao, Nonlinear lateral-torsional coupled motion of a rotor contacting a viscoelastically suspended stator. Nonlin. Dyn. 69 (2012): 325-339.

[53] H.M. Lankarani, P.E. Nikravesh, A contact force model with hysteresis damping for impact analysis of multibody systems. ASME J. Mech. Des 112 (1990) 369-376.

[54] H.M. Lankarani, P.E. Nikravesh, Continuous contact force models for impact analysis in multibody systems. Nonlin. Dyn. 5 (1994): 193-207.